Supporting information

UNDERSTANDING THE INTERNAL HEAVY-ATOM EFFECT ON THERMALLY ACTIVATED DELAYED FLUORESCENCE: APPLICATION OF ARRHENIUS AND MARCUS THEORIES FOR SPIN-ORBIT COUPLING ANALYSIS

Michał Mońka,[1] Illia E. Serdiuk[1],* Karol Kozakiewicz,[2] Estera Hoffman-Rusin,[1] Jan Szumilas,[1] Aleksander Kubicki,[1] Soo Young Park,[3] Piotr Bojarski[1]

[1] Faculty of Mathematics, Physics and Informatics, University of Gdańsk, Wita Stwosza 57, 80-308 Gdańsk, Poland

[2] Faculty of Chemistry, University of Gdańsk, Wita Stwosza 63, 80-308 Gdańsk, Poland

[3] Center for Supramolecular Optoelectronic Materials, Department of Materials Science and Engineering, Seoul National University, 1 Gwanak-ro, Gwanak-gu, Seoul 151-744, Republic of Korea

*Corresponding author. E-mail: illia.serdiuk@ug.edu.pl, phone + 48 58 523 22 44

Table of contents

Section S1. NMR spectra of target emitters

Figure S1. ^{1}H NMR spectrum of **diCl**

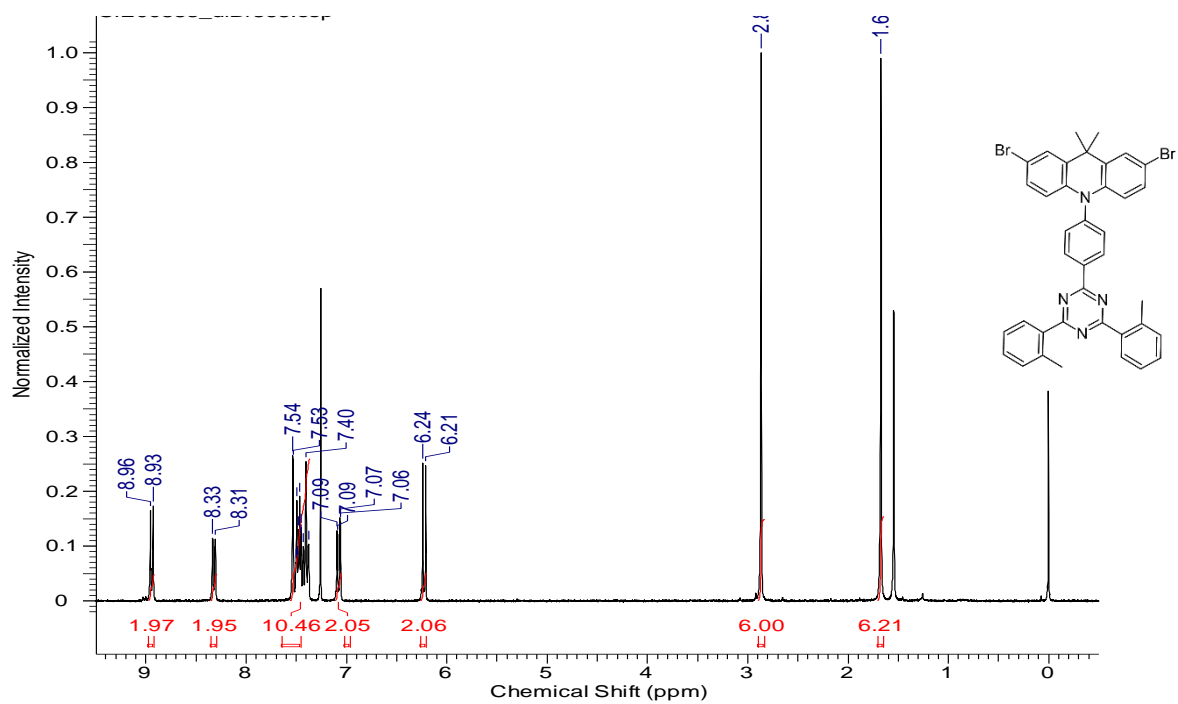**Figure S2.** ^{13}C NMR spectrum of **diCl**

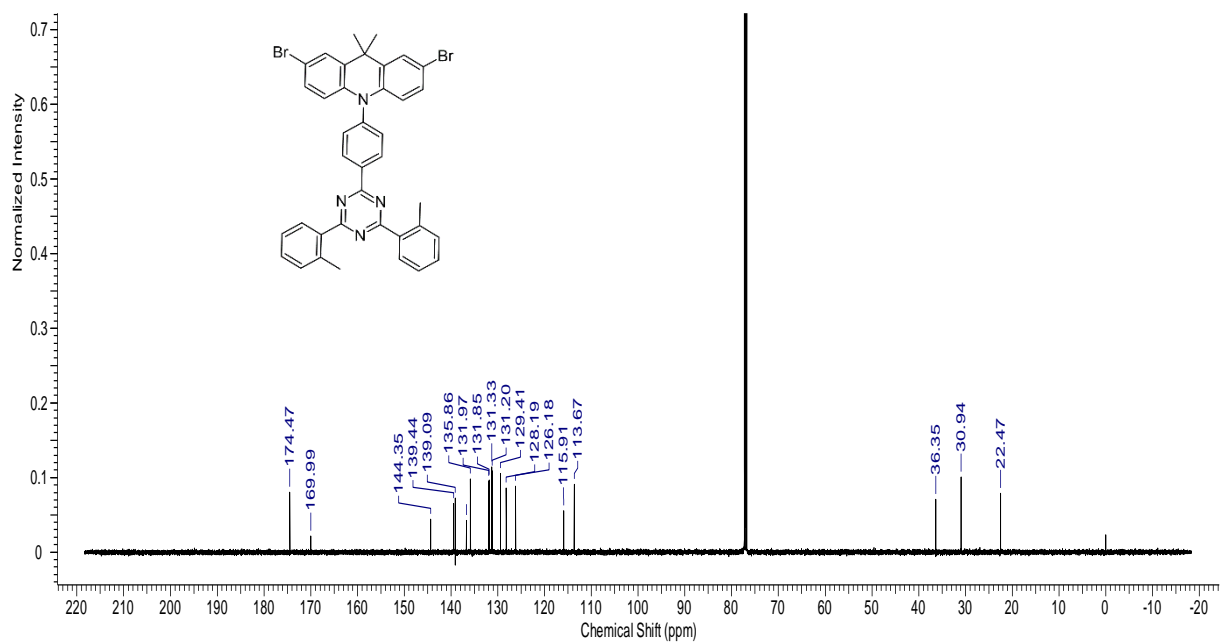**Figure S3.** ^{1}H NMR spectrum of **diBr**

**Figure S4.** ^{13}C NMR spectrum of **diBr**

S3

Section S2. Detailed discussion on spectral properties

Analysis of the nature of lowest excited electronic states on the basis of steady-state measurements. In nonpolar ZNX films at room temperature (RT), all three emitters (**H**, **diCl**, **diBr**) show vibronically-structured emission band with a maximum localized at 465–467 nm (**Figure 1C**). The onsets of fluorescence spectra (λ_{onset}, **Figures S6A-C**) were determined to be around 423, 418 and 421 nm for **H**, **diCl**, and **diBr**, respectively, which gives the S_1-state energies of 2.93, 2.97 and 2.95 eV, respectively (**Table S1**). In more polar PMMA, the emission becomes broad and structureless, and shifts to 492–499 nm range. The onsets of fluorescence in PMMA were estimated to be around $\lambda_{onset} = 430$, 427 and 428 nm for **H**, **diCl**, and **diBr** respectively (**Figures S6D-F**), which gives the energy levels of ^1CT states at 2.88, 2.90 and 2.89 eV. Such positive solvatofluorochromism typical for most of TADF emitters arises from the charge transfer (CT) character of the S_1-state [S1].

To reveal the nature and the energy of the lowest triplet excited states the phosphorescence measurements at low temperature were performed. As shown in **Figures S6A-C**, the phosphorescence spectrum of **H** in ZNX is red-shifted and has different shape as compared to that of fluorescence, with onset around $\lambda_{onset} = 437$ nm, which gives the energy level at 2.84 eV. The presented phosphorescence spectrum profile perfectly matches the shape of emission of the isolated acceptor fragment that was measured separately, as depicted in **Figure S6G**. Taking into account the previous studies of similar compound **DMAC-TRZ** [S2] our results indicate that the lowest triplet excited state of **H** in ZNX is of the localized nature (^3LE_A) originating from the acceptor fragment. The same conclusion was made for the **diCl** and **diBr** derivatives, as no significant differences in the phosphorescence spectra of **diCl** and **diBr** in ZNX were observed. In fact, as the halogens were introduced into donor fragment, they were not expected to affect the acceptor-localized ^3LE_A state. With respect to this, the energy gap $\Delta E_{1CT-3LE}$ between lowest excited singlet (^1CT) and triplet (^3LE_A) states in ZNX was estimated to be of 94, 133 and 114 meV for **H**, **diCl** and **diBr**, respectively (**Table S1**).

In more polar PMMA films, the phosphorescence spectrum of **H** broadens, becomes structureless and red-shifted as compared to the one measured in ZNX (**Figure S6D**). It should be noted, that in PMMA at 10K, to distinguish phosphorescence from the ^1CT-fluorescence, careful

analysis of TRES was conducted. As mentioned above, the specific feature of the ^{1}CT-fluorescence in DF region is its gradual blue-shift with the delay time. In PMMA films at 10K, the emission does not shift after the 50μs delay time (**Figure S8**). Its onset value in **H** falls around 443 nm, which is 0.04 eV below the ^{3}LE$_A$ state. Such observation indicates, that in PMMA phosphorescence occurs from the triplet charge-transfer (^{3}CT) state, energy of which is estimated around 2.80 eV. Similar observations for **diCl** and **diBr** gave the ^{3}CT levels of 2.81 eV (onset at 441 nm, **Figures S6E** and **S1F**). Taking into account these energies, the values of energy gap between lowest ^{1}CT and ^{3}CT states ($\Delta E_{1CT\text{-}3CT}$) were estimated as 85, 95 and 86 meV, as summarized in **Table 1.** Such relatively high values of $\Delta E_{1CT\text{-}3CT}$ are explained further.
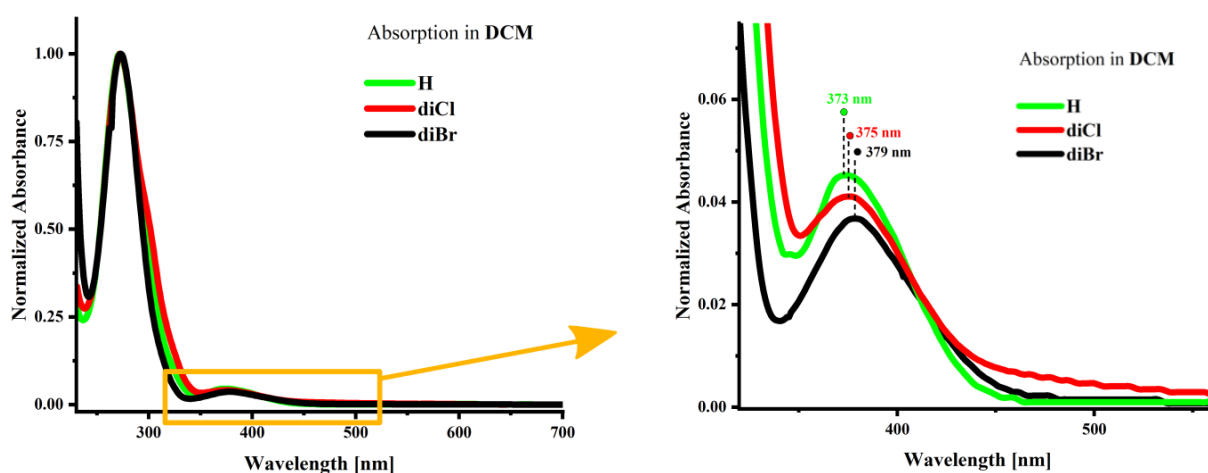
Figure S5. The absorption spectra of the investigated compounds measured in dichloromethane (DCM) solutions.
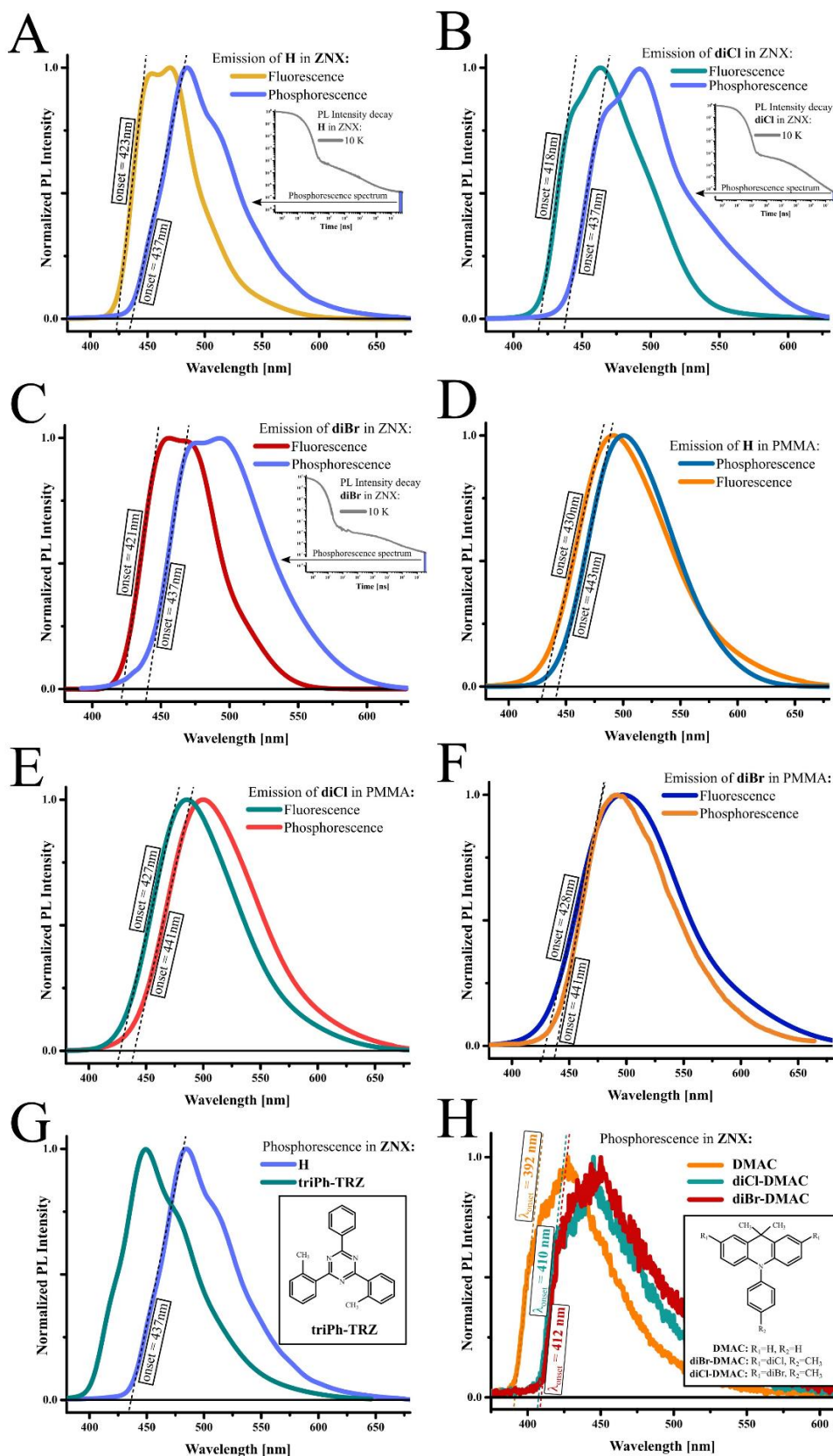
Figure S6. Steady-state fluorescence and phosphorescence spectra of **H**, **diCl** and **diBr** in ZNX (A, B, C, respectively) and in PMMA (D, E, F) with determined onsets. Fluorescence spectra were measured at room temperature in aerated conditions upon excitation λ_{exc}=370 nm. Phosphorescence spectra of isolated fragments: acceptor (G) and donors of **H**, **diCl** and **diBr** (H) were measured at 10 K with 30ms time delay under excitation λ_{exc}=320 nm.

Table S1. Photophysical parameters.

cmpd	medium	PLQY[a] [%]	Fluorescence ^{1}CT			Phosphorescence ^{3}LE(A)			Phosphorescence ^{3}CT			Phosphorescence ^{3}LE(D)			$\Delta E_{1CT\text{-}3LE(A)}$[e] [meV]	$\Delta E_{1CT\text{-}3CT}$[e] [meV]	$\Delta E_{1CT\text{-}3LE(D)}$[e] [meV]
			λ_{onset}[b] [nm]	Energy[c] [eV]	λ_{max}[d] [nm]	λ_{onset}[b] [nm]	Energy[c] [eV]	λ_{max}[d] [nm]	λ_{onset}[b] [nm]	Energy[c] [eV]	λ_{max}[d] [nm]	λ_{onset}[b] [nm]	Energy[c] [eV]	λ_{max}[d] [nm]			
H	ZNX	60	423	2.93	465	437	2.84	487	-	-	-	392	3.16	426	94	-	-230
diCl		75	418	2.97	462	437	2.84	489	-	-	-	410	3.02	447	133	-	-55
diBr		12	421	2.95	467	437	2.84	490	-	-	-	412	3.01	448	114	-	-55
H	PMMA	99	430	2.88	498	-	-	-	443	2.80	498	-	-	-	46	85	-278
diCl		85	427	2.90	492	-	-	-	441	2.81	494	-	-	-	72	95	-116
diBr		21	428	2.89	499	-	-	-	441	2.81	500	-	-	-	60	86	-109

[a] - PLQY was measured at 298K using integrating sphere under oxygen atmosphere. The values presented in the table are corrected for vacuum conditions according to proportional relationship: PLQY = $PLQY_{air}$ x ($DecArea_{vac}/DecArea_{air}$), where $PLQY_{air}$ is value obtained under oxygen atmosphere, $DecArea_{vac}$ and $DecArea_{air}$ are total areas under PL intensity decays measured in vacuum and under oxygen atmosphere, respectively (**Figure S7A-F**);

[b] - onsets determined experimentally from PL spectra (see **Figure S6A-F** for ^{1}CT, **Figures S6A-C** and **S6G** for ^{3}LE(A), **Figure S6H** for ^{3}LE(D) and **Figure S6D-F** for ^{3}CT-state);

[c] - energies of respective excited states calculated from relation: $E = 1240/\lambda_{onset}$;

[d] – photoluminescence maxima (see **Figure S6** for ^{1}CT and ^{3}LE(A), **Figures S6H** for ^{3}LE(D) and **Figures S6D-F** for ^{3}CT-state);

[e] - energy gap determined from the difference of respective onsets of PL spectra: $\Delta E_{1\text{-}2} = (1240/\lambda_{onset1} - 1240/\lambda_{onset2})$.

Time-resolved emission spectra and emission decays

As can be seen in **Figure S7**, the PL decay for each of studied emitters contains two well-separated areas in nano- and microsecond regimes corresponding to the prompt and delayed emission. The PL intensity decay profiles measured in the presence of oxygen differ from those recorded in the vacuum due to quenching by molecular oxygen, which confirms that TADF is mediated by triplet state(s).
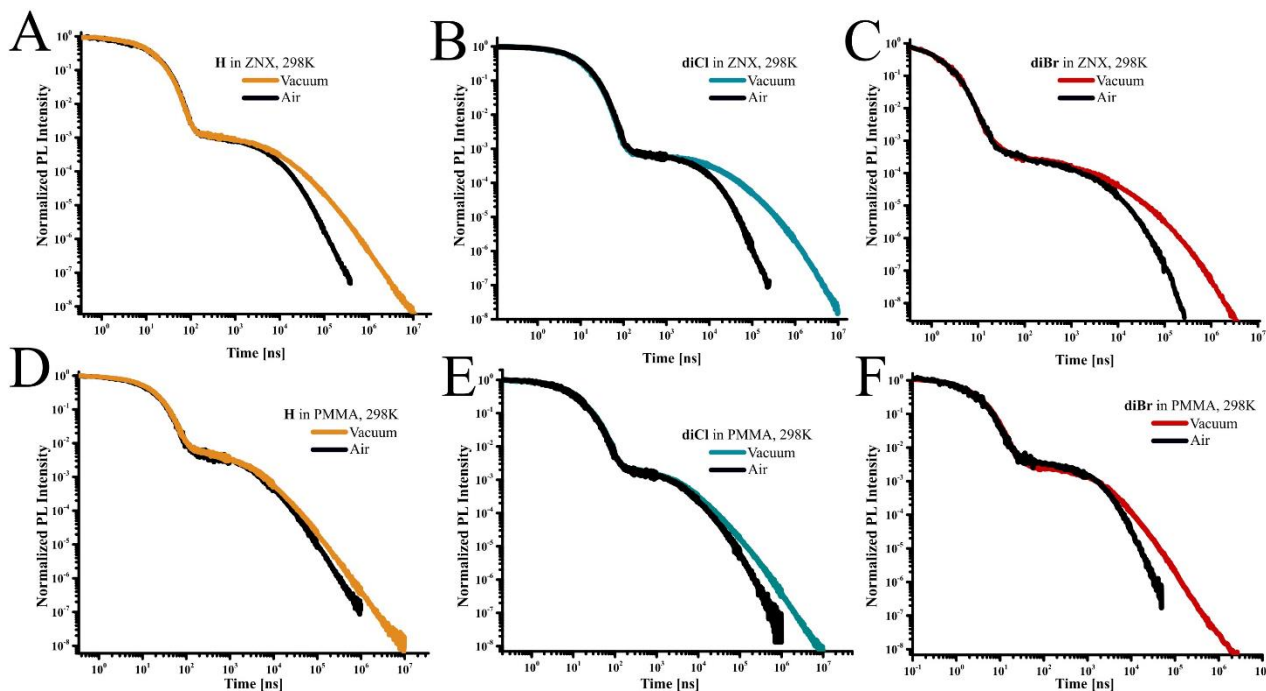
Figure S7. Time-resolved PL measurements of studied compounds dispersed in ZNX (A-C) and PMMA (D-F) in the presence of oxygen and in vacuum at 298 K. Excitation wavelength λ_{exc}=370 nm.

To verify whether the delayed emission originates from the ^{1}CT-state, detailed time-dependent analysis of PL spectra was carried out (**Figures S8A** and **S9A**). Through the entire timescale of PL spectra of each emitter, all the collected spectra have roughly similar shape and maximum (**Figures S8B-D**, **S9B-D**). Therefore, the fast component can be identified as prompt fluorescence (PF), occurring from the directly excited ^{1}CT-state, whilst the slow one is due to the delayed fluorescence (DF), where emission from the ^{1}CT-state is preceded by ISC and rISC.

For time-resolved emission spectra (TRES) in PF region over the first 100 ns, the emission maximum red-shifts from 452 to 463 nm in ZNX and 473 to 497 nm in PMMA (**Figures S8-S11**). In

the DF regime starting from 1 μs, TRES undergo the red shift from 455 nm to 481 nm. Such spectral behavior can be explained by the distribution of ^{1}CT states due to the coexistence of different emitter conformations. As suggested in previous reports[S2, S3], the most crucial conformers differ by the dihedral angle between donor and acceptor units (θ, **Figures 1B** and **1D**, main text). At the very early stages of PF, the blue-shifted fluorescence spectrum originates from the conformers with the most deviated θ-value from the optimal 90°. The deviation from orthogonality leads to the increased overlap of molecular orbitals (MOs) involved in the CT transition, and thus better conjugation of donor and acceptor fragments. For this reason, such conformers have higher energies of ^{1}CT states and higher value of S_1-S_0 oscillator strength, which enables relatively fast emission. As θ approaches to orthogonal, the ^{1}CT state becomes more stabilized due to decreased conjugation between D and A, which leads to red-shift of emission and lower S_1-S_0 oscillator strengths. Such conformers emit at the late PF. The opposite behavior is observed for the DF region. The red-shifted emission is responsible for the early-DF, whilst in the late-DF blue shift is observed. As the most orthogonal conformers have the smallest energy gap between singlet and triplet state ΔE_{ST}, which according to Marcus-Hush equation (eq. 2 in main text) leads to the highest rISC rates, their red-shifted DF appears first. Consequently, as the θ-deviation increases, ΔE_{ST} increases too, rISC becomes slower and the DF spectrum gradually shifts to shorter wavelengths.

The distribution of ^{1}CT-state energy and relatively constant energy of the ^{3}CT-state (**Figure S12A-C**), explains relatively high values of $\Delta E_{1CT-3CT}$ mentioned above.
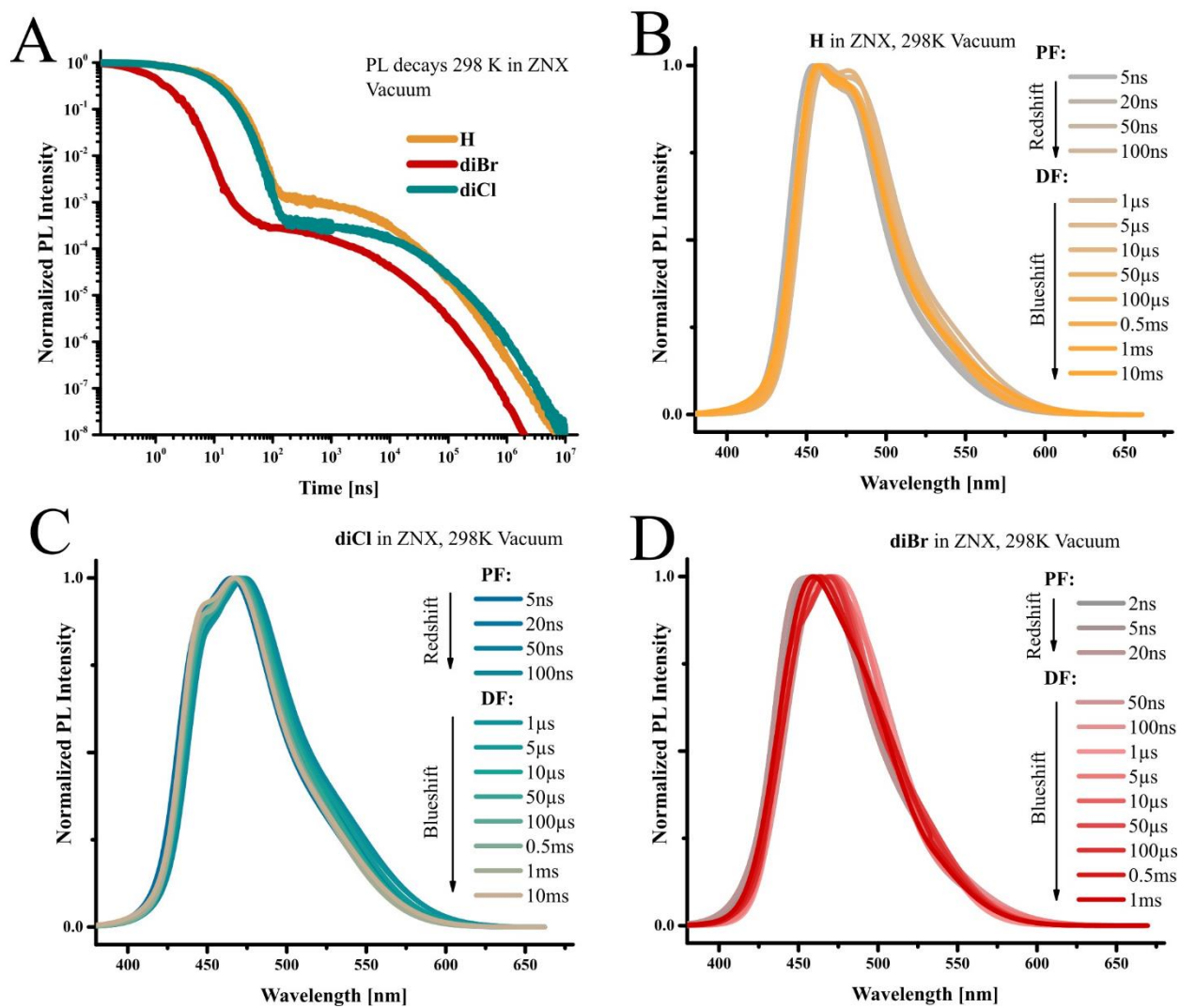
Figure S8. PL intensity decay profiles of **H**, **diCl**, and **diBr** in ZNX (A) with PL spectra taken at different time delays (B-D). Excitation wavelength λ_{exc}=370 nm.
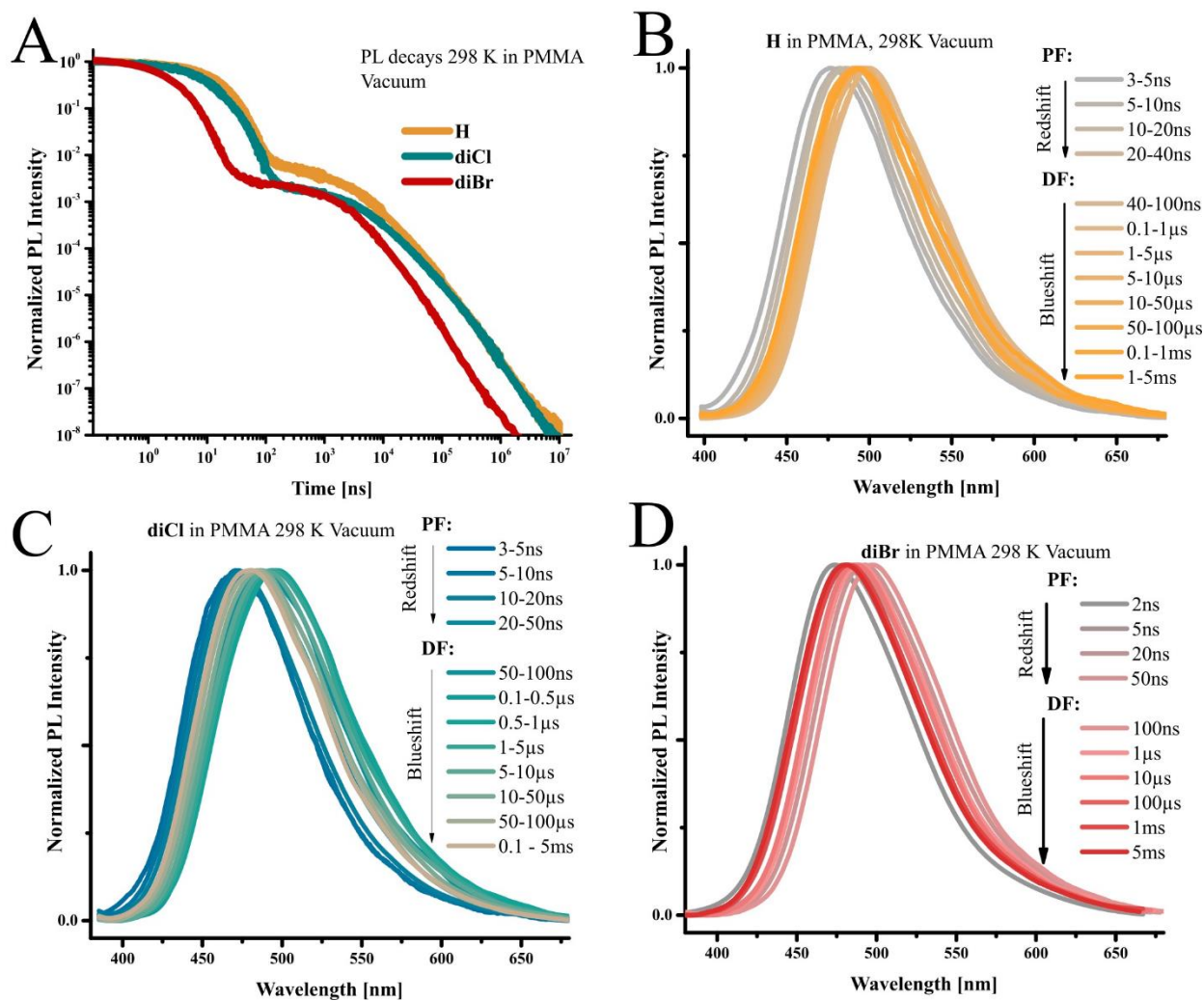
Figure S9. PL intensity decay profiles of **H**, **diCl**, and **diBr** in PMMA (A) with PL spectra taken at different time delays (B-D). Excitation wavelength λ_{exc}=370 nm.
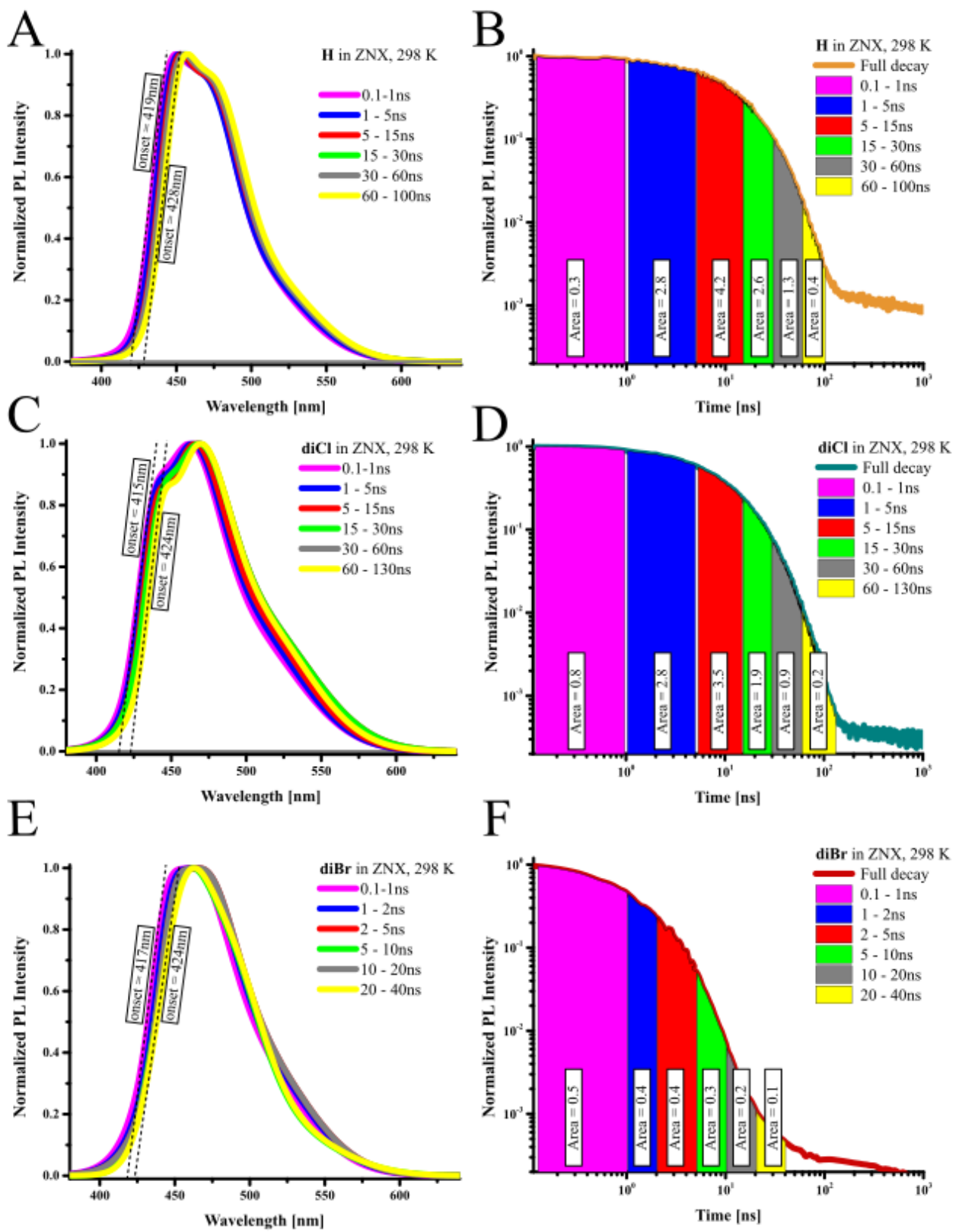
Figure S10. Time evolution of PL spectra within PF of **H, diCl** and **diBr** (A, C, E) with corresponding time frames (B, D, F) in ZNX measured at 298 K in vacuum. Excitation wavelength λ_{exc}=370 nm.
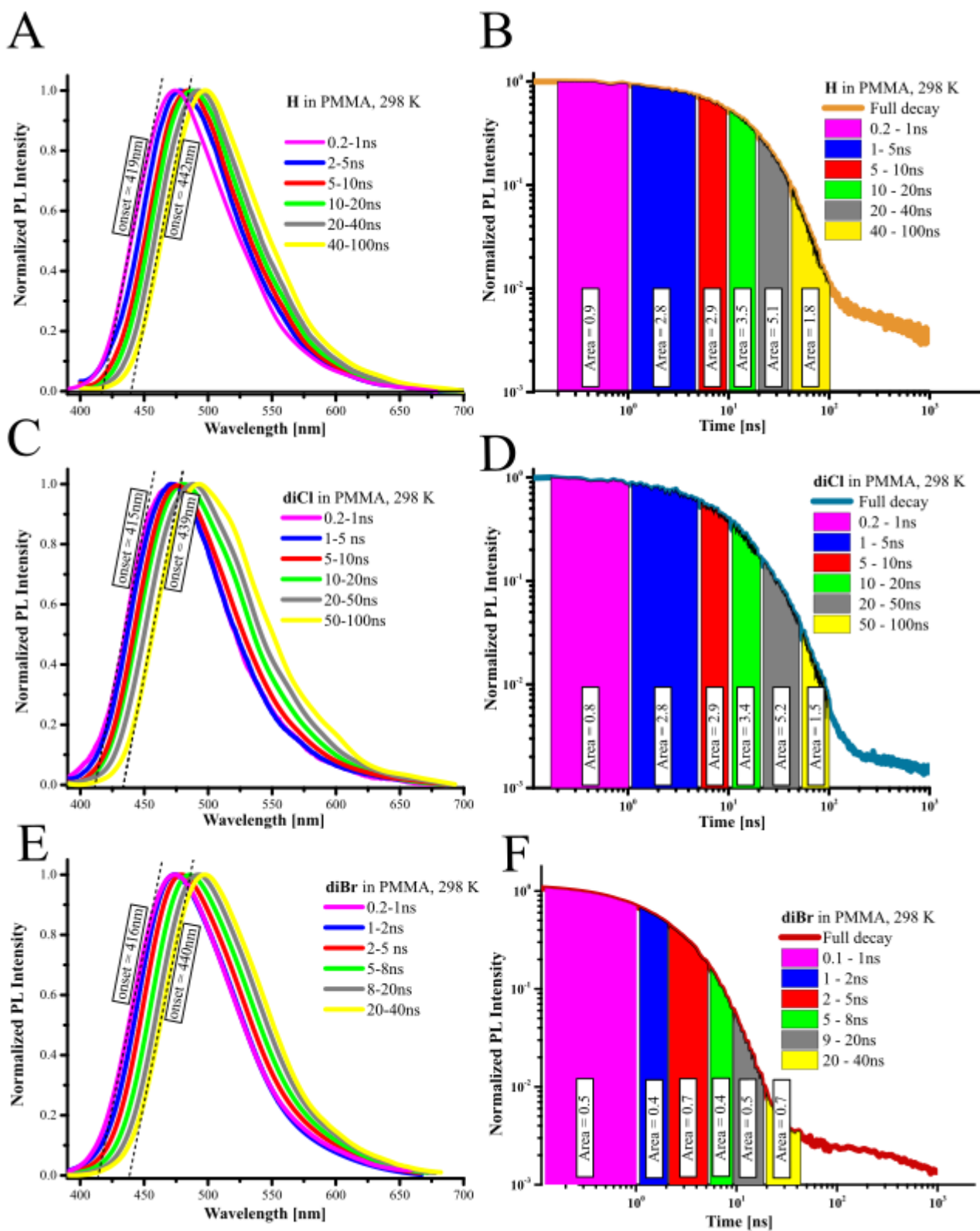
Figure S11. Time evolution of PL spectra within PF region of **H, diCl** and **diBr** (A, C, E) with corresponding time frames (B, D, F) in PMMA measured at 298 K in vacuum. Excitation wavelength λ_{exc}=370 nm.

Table S2. Experimental determination of minimal, maximal and statistically mean ^{1}CT-onset values

cmpd	Figures[a]	medium		Time [ns]	Onset [nm]	Energy [eV][b]	Area[c]	Contribution [%]
H	**S10A, S10B**	ZNX		0.2-1	419	2.96	0.7	5.8
				1-5	420	2.95	2.8	23.2
				5-15	423	2.93	4.2	35.0
				15-30	424	2.92	2.6	21.7
				30-60	427	2.90	1.3	11.0
				60-100	428	2.90	0.4	3.4
				Weighted average	**423**	**2.93**		
diCl	**S10C, S10D**	ZNX		0.2-1	415	2.96	0.8	7.9
				1-5	416	2.95	2.8	27.8
				5-15	418	2.93	3.5	34.0
				15-30	420	2.92	1.9	19.1
				30-60	422	2.90	0.9	9.1
				60-100	424	2.90	0.2	2.0
				Weighted average	**418**	**2.97**		
diBr	**S10E, S10F**	ZNX		0.1-1	417	2.97	0.5	26.1
				1-2	420	2.95	0.4	21.6
				2-5	421	2.95	0.4	21.0
				5-10	422	2.94	0.3	15.9
				10-20	423	2.93	0.3	10.6
				20-40	424	2.92	0.1	5.3
				Weighted average	**421**	**2.95**		
H	**S11A, S11B**	PMMA		0.2-1	419	2.96	0.9	5.1
				2-5	421	2.95	2.8	16.1
				5-10	424	2.92	2.9	16.8
				10-20	428	2.90	3.5	20.5
				20-40	437	2.84	5.1	30.5
				40-100	442	2.81	1.8	10.9
				Weighted average	**430**	**2.88**		
diCl	**S11C, S11D**	PMMA		0.2-1	415	2.99	0.8	4.9
				1-5	417	2.97	2.8	17.3
				5-10	420	2.95	2.9	17.8
				10-20	427	2.90	3.4	20.5
				20-50	433	2.86	5.2	30.9
				40-100	439	2.82	1.5	8.8
				Weighted average	**427**	**2.91**		
diBr	**S11E, S11F**	PMMA		0.2-1	416	2.98	0.5	15.2
				1-2	419	2.96	0.4	12.3
				2-5	422	2.94	0.7	21.5
				5-8	429	2.89	0.4	12.5
				8-20	438	2.83	0.5	16.0
				20-40	440	2.82	0.7	22.4
				Weighted average	**428**	**2.90**		

[a] – Figures demonstrating integration ranges and corresponding PL spectra;

[b] – Energy calculated from relation: $E = 1240/\lambda_{onset}$;

[c] – Area obtained by integration of PL decay curve over specified time interval, as depicted in respective figures[a].

Table S3. Minimal, maximal, and statistically mean values of energy gaps.

		$\Delta E_{1CT-3CT}$ [meV]			$\Delta E_{1CT-3LE(A)}$ [meV]			$\Delta E_{1CT-3LE(D)}$ [meV]		
		Min	Mean	Max	Min	Mean	Max	Min	Mean	Max
H	PMMA	6	85	160	-32	46	121	-203	-278	-357
diCl	PMMA	13	95	176	-10	72	153	-35	-116	-198
diBr	PMMA	6	86	169	-20	60	143	-24	-109	-189
H	ZNX				59	94	121	-203	-230	-265
diCl	ZNX				90	133	153	-35	-55	-99
diBr	ZNX				86	114	143	-27	-55	-83

Energy gaps were determined from the difference of respective onsets of PL spectra, according to general equation: $\Delta E_{1-2} = (1240/\lambda_{onset1} - 1240/\lambda_{onset2})$.
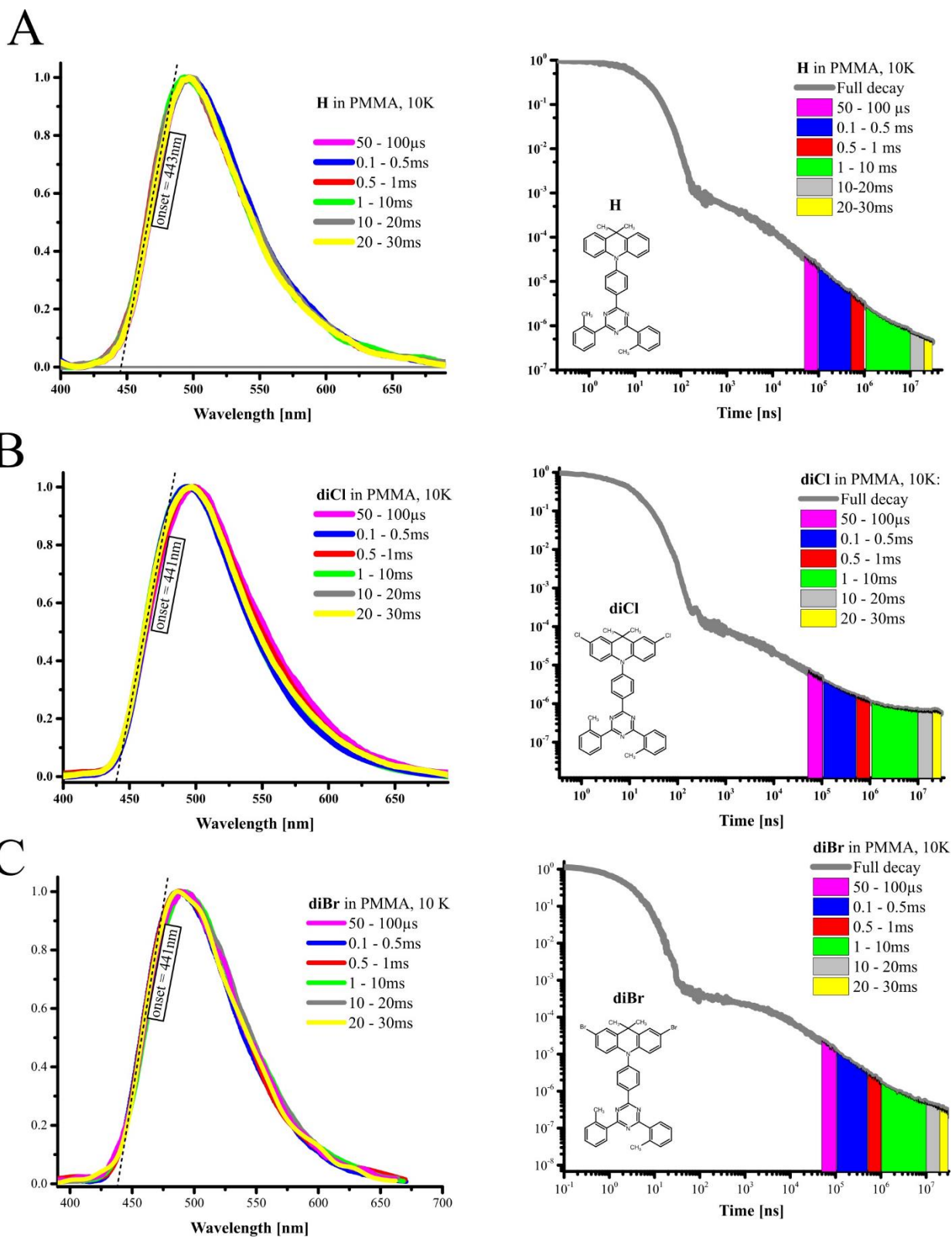
Figure S12. PL intensity decay profiles of **H**, **diCl**, and **diBr** in PMMA with PL spectra taken at different time delays measured at 10 K. Excitation wavelength $\lambda_{exc}=370$ nm.

Section S3: Determination of photophysical parameters

PL decay curves (presented in **Figures S8A, S9A** and **S13**) were fitted with the multiexponential equation:

$$I(t) = A_0 + \sum_{i=1}^{n} A_i \exp\left(-t/\tau_i\right) \tag{S1}$$

where A_i is the pre-exponential factor, τ_i is the decay time and $I(t)$ is emission intensity. Average lifetimes of prompt (τ_{PF}) and delayed fluorescence (τ_{DF}) were determined using the following formula:

$$\tau_{PF}, \tau_{DF} = \sum_{i=1}^{n} f_i \tau_i, \tag{S2}$$

where f_i is fractional contribution of i-th component expressed as:

$$f_i = \frac{A_i \tau_i}{\sum_{i=1}^{n} A_i \tau_i} \tag{S3}$$

The ratio of DF and PF quantum yields $\varphi_{DF}/\varphi_{PF}$ was determined as follows [S4]:

$$\frac{\varphi_{DF}}{\varphi_{PF}} = \frac{\sum_{i=1}^{n} \tau_{DF(i)} A_{DF(i)}}{\sum_{j=1}^{n} \tau_{PF(j)} A_{PF(j)}} \tag{S4}$$

where $A_{DF(i)}$ and $A_{PF(j)}$ is the pre-exponential factor of delayed and prompt fluorescence component, respectively; $\tau_{DF(i)}$ and $\tau_{PF(j)}$ is the lifetime of delayed and prompt fluorescence component, respectively. The rate constants of radiative (k_r) and nonradiative (k_{nr}) decay and intersystem crossing (k_{ISC}) are given by equations:

$$k_r = \frac{\varphi_{PF}}{\tau_{PF}}, \tag{S5}$$

$$k_{ISC} = \frac{\varphi_{DF}}{\varphi\, \tau_{PF}}, \tag{S6}$$

$$k_{nr} = \frac{1}{\tau_{PF}} - (k_r + k_{ISC}). \tag{S7}$$

where φ is PLQY $(\varphi_{DF} + \varphi_{PF})$. Further, the quantum yields for ISC and rISC were calculated as

$$\varphi_{ISC} = k_{ISC}\tau_{PF}, \tag{S8}$$

$$\varphi_{rISC} = \frac{1 - \varphi_{PF}/\varphi}{\varphi_{ISC}}. \tag{S9}$$

Finally, the rate constant of rISC (k_{rISC}) was calculated as

S17

$$k_{rISC} = \frac{\varphi_{rISC}}{\tau_{DF}}\left(\frac{\varphi}{\varphi_{PF}}\right). \tag{S10}$$

Photophysical parameters are presented in **Tables 1** (main text) and **S4**.

Table S4. Experimentally determined photophysical parameters.

Cmpd	medium	φ_{PF}	φ_{DF}	$\varphi_{DF}/\varphi_{PF}$	τ_{PF}	τ_{DF}	k_r	k_{ISC}	k_{rISC}
		[%]	[%]		[ns]	[µs]	[s^{-1} 10^7]	[s^{-1} 10^7]	[s^{-1} 10^4]
H	ZNX	22.1	27.9	1.3	15.3	171	1.5	5.1	1.03
diCl		21.6	53.2	2.5	13.1	333	1.8	6.1	0.87
diBr		4.5	6.5	1.4	2.2	104	2.0	38.5	1.74
H	PMMA	33.4	63.3	1.8	17.1	96	2.1	3.8	2.92
diCl		32.4	53.1	1.6	16.0	139	2.0	4.1	1.85
diBr		5.7	15.1	2.7	2.8	38	2.0	30.8	8.23

Section S4: Temperature-dependent time-resolved analysis based on Arrhenius and Marcus theories

Time-resolved PL measurements were conducted within the temperature range of 298–10 K (**Figure S13**). The PL decays in the 298 – 150 K range contained only prompt and delayed fluorescence, thus phosphorescence did not interfered. The latter temperature range was thus used for further investigations. The PL decay analysis as described in section S3 enabled k_{ISC} and k_{rISC} constant rates at various temperatures (**Tables S5, S6**). To determine the energy barriers E_a for ISC and rISC, the Arrhenius law equation was applied:

$$k_{(r)ISC} = A \cdot \exp\left(-\frac{E_a}{k_B T}\right), \tag{S11}$$

where k_B stands for Boltzmann constant, and A is pre-exponential constant (**Table 2,** main text).
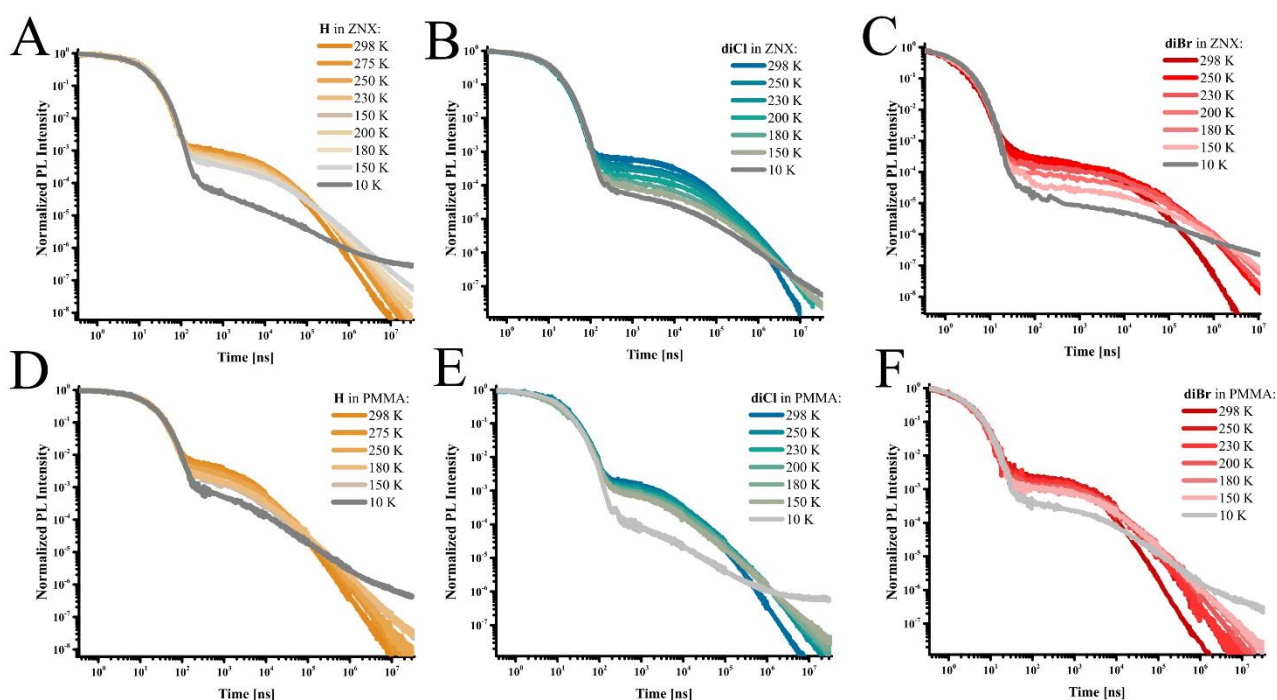
Figure S13. PL intensity decay profiles of **H**, **diCl**, and **diBr** in ZNX (A-C) and PMMA (D-F) conducted in various temperatures within 298-10 K. Excitation wavelength λ_{exc}=370 nm.

Table S5. Photophysical parameters in ZNX at various temperatures with corresponding linear regression parameters.

	T [K]	τ_{PF}^{b} [ns]	τ_{DF}^{b} [μs]	k_r 10^7 [s^{-1}]	k_{ISC} 10^7 [s^{-1}]	k_{nr} 10^7 [s^{-1}]	k_{rISC} 10^4 [s^{-1}]	ln(k_{ISC})	ln(k_{rISC})
H	298	15.3	171	1.5	5.1	0.0	1.03	17.7	9.16
	275	15.3	376	1.5	5.1	0.0	0.58	17.7	8.67
	250	15.3	724	1.5	5.1	0.0	0.30	17.7	7.98
	230	15.3	806	1.5	5.1	0.0	0.24	17.7	7.78
	200	15.3	2328	1.5	5.1	0.0	0.08	17.7	6.71
	180	15.3	6799	1.5	5.1	0.0	0.03	17.7	5.67
	150	15.3	30855	1.5	5.1	0.0	0.01	17.7	4.31

Parameters of linear regression for rISC derived from (S11):

Slope	1447
Intercept	14.02
E_a [meV]	124
A [s^{-1} 10^7]	0.12

	T [K]	τ_{PF}^{b} [ns]	τ_{DF}^{b} [μs]	k_r 10^7 [s^{-1}]	k_{ISC} 10^7 [s^{-1}]	k_{nr} 10^7 [s^{-1}]	k_{rISC} 10^4 [s^{-1}]	ln(k_{ISC})	ln(k_{rISC})
diCl	298	12.9	333	1.7	6.1	0.0	0.87	17.9	9.1
	250	12.8	1167	1.7	6.1	0.0	0.27	17.9	7.9
	230	12.9	1547	1.7	6.1	0.0	0.17	17.9	7.4
	200	12.9	3013	1.7	6.1	0.0	0.08	17.9	6.7
	180	12.9	6658	1.7	6.1	0.0	0.02	17.9	5.5
	150	13.0	17755	1.7	6.1	0.0	0.01	17.9	4.5

Parameters of linear regression for rISC derived from (S11):

Slope	1475
Intercept	13.71
E_a [meV]	127
A [s^{-1} 10^7]	0.09

	T [K]	τ_{PF}^{b} [ns]	τ_{DF}^{b} [μs]	k_r 10^7 [s^{-1}]	k_{ISC} 10^7 [s^{-1}]	k_{nr} 10^7 [s^{-1}]	k_{rISC} 10^4 [s^{-1}]	ln(k_{ISC})	ln(k_{rISC})
diBr	298	2.2	104	2.0	38.5	3.8	1.74	19.7	9.7
	250	2.2	816	2.0	38.5	1.8	0.56	19.7	8.6
	230	2.3	1435	2.0	38.5	1.7	0.29	19.7	7.9
	180	2.3	9272	2.0	38.5	1.2	0.05	19.7	6.2
	150	2.3	32595	2.0	38.5	0.4	0.01	19.7	4.9

Parameters of linear regression for rISC derived from (S11):

Slope	1443
Intercept	14.31
E_a [meV]	125
A [s^{-1} 10^7]	0.16
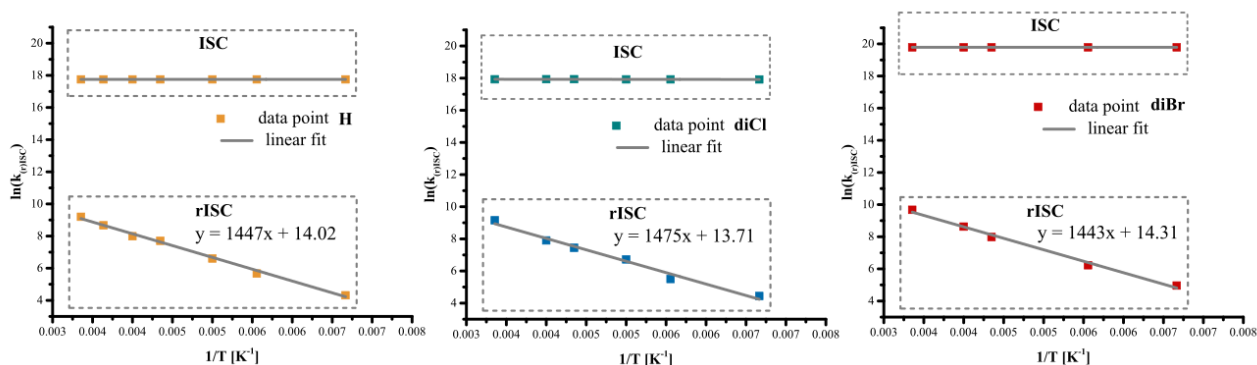
Figure S14. Arrhenius plots for emitters dispersed in ZNX.

Table S6. Photophysical parameters in PMMA at various temperatures with corresponding linear regression parameters.
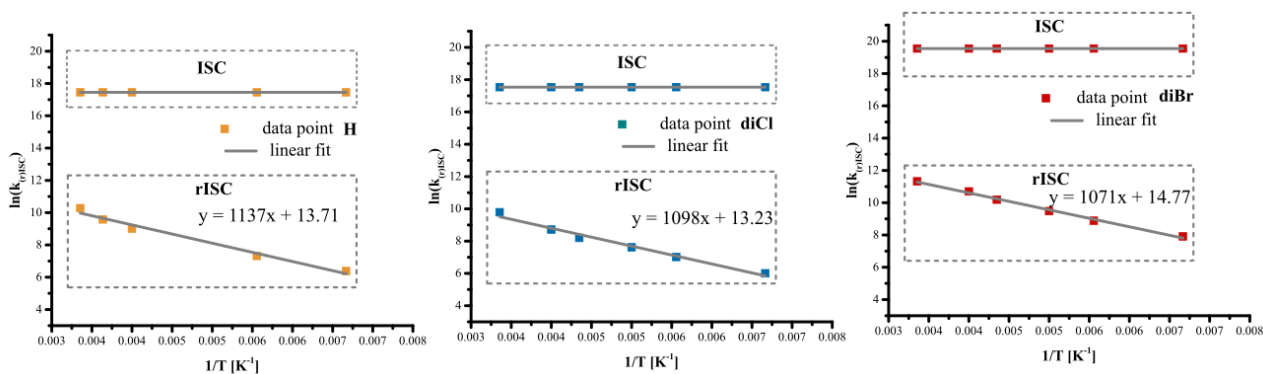
PMMA								
H T [K]	$\tau_{PF}{}^b$ [ns]	$\tau_{DF}{}^b$ [µs]	k_r 10^7 [s^{-1}]	k_{ISC} 10^7 [s^{-1}]	k_{nr} 10^7 [s^{-1}]	k_{rISC} 10^4 [s^{-1}]	ln(k_{ISC})	ln(k_{rISC})
298	17.2	96	2.0	3.8	0.04	2.92	17.4	10.1
275	17.1	188	2.1	3.8	0.03	1.45	17.4	9.6
250	17.1	328	2.1	3.8	0.02	0.82	17.4	9.0
180	17.2	1773	2.0	3.8	0.01	0.15	17.4	7.3
150	17.1	4357	2.1	3.8	0.00	0.06	17.4	6.4

Parameters of linear regression for rISC derived from (S11):

Slope	1137
Intercept	13.71
E_a [meV]	98
A [s^{-1} 10^7]	0.09

diCl T [K]	$\tau_{PF}{}^b$ [ns]	$\tau_{DF}{}^b$ [µs]	k_r 10^7 [s^{-1}]	k_{ISC} 10^7 [s^{-1}]	k_{nr} 10^7 [s^{-1}]	k_{rISC} 10^4 [s^{-1}]	ln(k_{ISC})	ln(k_{rISC})
298	16.0	139	2.1	4.1	0.11	1.85	17.5	9.8
250	16.0	431	2.1	4.1	0.10	0.67	17.5	8.7
230	16.0	701	2.1	4.1	0.08	0.36	17.5	8.2
200	15.9	1165	2.2	4.1	0.06	0.20	17.5	7.6
180	16.1	2050	2.1	4.1	0.03	0.11	17.5	7.0
150	16.1	5392	2.1	4.1	0.01	0.04	17.5	6.0

Parameters of linear regression for rISC derived from (S11):

Slope	1098
Intercept	13.23
E_a [meV]	95
A [s^{-1} 10^7]	0.06

diBr T [K]	$\tau_{PF}{}^b$ [ns]	$\tau_{DF}{}^b$ [µs]	k_r 10^7 [s^{-1}]	k_{ISC} 10^7 [s^{-1}]	k_{nr} 10^7 [s^{-1}]	k_{rISC} 10^4 [s^{-1}]	ln(k_{ISC})	ln(k_{rISC})
298	2.6	38	2.1	30.8	3.1	8.23	19.5	11.2
250	2.6	110	2.1	30.8	2.9	4.43	19.5	10.7
230	2.6	179	2.0	30.8	2.8	2.26	19.5	10.1
200	2.6	386	2.1	30.8	2.0	1.30	19.5	9.5
180	2.8	672	2.0	30.8	1.8	0.72	19.5	8.9
150	2.8	1738	2.0	30.8	1.5	0.27	19.5	7.9

Parameters of linear regression for rISC derived from (S11):

Slope	1071
Intercept	14.77
E_a [meV]	92
A [s^{-1} 10^7]	0.26

Figure S15. Arrhenius plots for emitters dispersed in PMMA.

More detailed information can be derived using the Marcus-Hush equation:

$$k_{(r)ISC} = \frac{V^2}{\hbar} \sqrt{\frac{\pi}{k_B T \lambda}} \exp\left[-\frac{(\Delta E_{ST} + \lambda)^2}{4 k_B T \lambda}\right],$$ (S12)

where V is SOC constant, $\hbar$ is reduced Planck's constant, λ is sum of internal and external (λ_{solv}) reorganization energies for respective transition, ΔE_{ST} is the energy gap between singlet ^1CT and respective triplet state. This semiclassical expression, commonly used to predict constant rates for non-radiative transitions in D-A structure of TADF compounds can be connected with the Arrhenius equation (S11) by the following relations:

$$A = \frac{V^2}{\hbar} \sqrt{\frac{\pi}{k_B T \lambda}},$$ (S13)

$$E_a = \frac{(\Delta E_{ST} + \lambda)^2}{4\lambda}.$$ (S14)

Consequently, by matching the ΔE_{ST} and λ parameters to satisfy both relations, where E_a and A are derived from Arrhenius plot, it is possible to estimate empirical SOC values V for each transition, as it is presented in **Table 2** (main text).

As discussed in main text, because ISC transition does not require thermal activation under all conditions investigated ($E_a = 0$), the relation (S14) predicts the same values of ΔE_{ST} and λ:

$$\Delta E_{ST} = \lambda.$$ (S15)

Assuming equal values of ΔE_{ST} for both ISC and rISC (S6):

$$\Delta E_{ST}(ISC) = -\Delta E_{ST}(rISC),$$ (S16)

the ΔE_{ST} and λ values can be obtained from eq. (S14) and E_a (**Table 2**). The V_{ISC} and V_{rISC} parameters are then available from eq. (S14) and A (**Table 2**):

(S17)

$$A_{ISC} = \frac{V_{ISC}^2}{\hbar} \sqrt{\frac{\pi}{k_B T \lambda}},$$

$$A_{rISC} = \frac{V_{rISC}^2}{\hbar} \sqrt{\frac{\pi}{k_B T \lambda}}. \tag{S18}$$

The assumption (S16) seems to be valid because regardless of the ISC and rISC mechanism, the $\Delta E_{1CT-3CT}$ and $\Delta E_{1CT-3LE(A)}$ values were determined to be similar (**Table 1**). On the other hand, the changes in the obtained V_{ISC} and V_{rISC} values are much greater than those in ΔE_{ST}. Therefore, the assumption (S16) introduces minor uncertainty and does not affect the most important conclusions made for ISC and rISC mechanisms.

Test for the comparability of the investigated emitters. In an ideal case, to compare different emitters under the conditions of isomeric inhomogeneity, same kinds of their rotational and vibrational isomers should be taken into account in the similar amounts. To check if this criterion is fulfilled the analysis of Arrhenius plot can be performed. In the current example, despite the fact that the k_{nr} values are different under various temperatures, their change does not affect the dependence of k_{rISC} on $1/T$: 1) the $k_{rISC}(1/T)$ dependence remains linear for all the investigated temperature range; 2) the slope of the $k_{rISC}(1/T)$ dependence is almost identical for all three compounds (Figures S14 and S15). This means that all kinds of the rotational and vibrational isomers are represented under various temperatures and in all three compounds. None of the rotational and vibrational isomers are added or eliminated under the change of temperature. In other words, the investigated molecular systems are totally comparable but represent with different emission intensity due to different PLQY.

Strong temperature dependence of k_{nr} in both **diCl** and **diBr**, evidence that main nonradiative deactivation channel can be activated by the molecular vibrations involving heavy atom(s). However, good photochemical stability of the investigated samples under experimental conditions, i.e. irradiation with 10 mJ laser beam, indicates the breakage of neither C–Br nor C–Cl bond is responsible for the non-radiative deactivation.

Section S5: Theoretical prediction of ISC and rISC rate constants for the ^{1}CT-^{3}LE transitions

Calculations for ISC rate constants. Theoretical rate constants of ISC and rISC were calculated using Marcus-Hush equation (S12). According to the IUPAC definition, [S5] term reorganization energy λ corresponds to the energy that is dissipated by molecule that underwent vertical excitation, when relaxing to the equilibrium state for its new charge distribution. Commonly, total λ is a sum of inner (λ_{in}) and outer (λ_{out}) reorganization energies:

$$\lambda = \lambda_{in} + \lambda_{out}. \tag{S19}$$

By performing single-point TD-DFT calculations for **H**, **diCl** and **diBr**, we determined the values of inner reorganization energies λ_{in} for each ISC transition, namely:

- ^{1}CT $\rightarrow$ ^{3}LE(A): $\lambda_{in} = \lambda_{1CT \rightarrow 3LE(A)}$

- ^{1}CT $\rightarrow$ ^{3}LE(D): $\lambda_{in} = \lambda_{1CT \rightarrow 3LE(D)}$

using the following formulas:

$$\lambda_{1CT \rightarrow 3LE(A)} = E^{1CT}_{3LE(A)} - E^{3LE(A)}_{3LE(A)}, \tag{S20}$$

$$\lambda_{1CT \rightarrow 3LE(D)} = E^{1CT}_{3LE(D)} - E^{3LE(D)}_{3LE(D)}, \tag{S21}$$

where:

$E^{1CT}_{3LE(A)}$ - TD-DFT energy of ^{3}LE(A) excited state at the ^{1}CT optimized geometry

$E^{3LE(A)}_{3LE(A)}$ - TD-DFT energy of ^{3}LE(A) excited state at the ^{3}LE(A) optimized geometry

$E^{1CT}_{3LE(D)}$ - TD-DFT energy of ^{3}LE(D) excited state at the ^{1}CT optimized geometry,

$E^{3LE(D)}_{3LE(D)}$ - TD-DFT energy of ^{3}LE(D) excited state at the ^{3}LE(D) optimized geometry.

The λ_{out} value of 0.05 eV was used for all calculations.

Since DFT fails to predict ΔE_{ST}, the experimentally determined mean values of $\Delta E_{1CT\text{-}3LE(A)}$ and $\Delta E_{1CT\text{-}3LE(D)}$ were used (**Table 1**, main text).

Computed reorganization energies for respective ISC transitions:

	$^1CT \to {}^3LE(A)$			$^1CT \to {}^3LE(D)$:		
	$E_{3LE(A)}^{1CT}$	$E_{3LE(A)}^{3LE(A)}$	$\lambda_{1CT \to 3LE(A)}$	$E_{3LE(D)}^{1CT}$	$E_{3LE(D)}^{3LE(D)}$	$\lambda_{1CT \to 3LE(D)}$
cmpd	[a. u]	[a. u]	[eV]	[a. u]	[a. u]	[eV]
H	-1607.3656182	-1607.3715987	0.17	-1607.3509293	-1607.3594832	0.23
diCl	-1636.0412315	-1636.0470891	0.16	-1636.0292145	-1636.0381835	0.24
diBr	-1632.4758713	-1632.4840055	0.22	-1632.4653425	-1632.4757523	0.28

Table S7. Computational data for prediction ISC constant rate within $^1CT \to {}^3LE(A)$ transition

		$V_{1CT \to 3LE(A)}{}^{a}$	$\lambda_{1CT \to 3LE(A)}{}^{b}$	$\Delta E_{1CT\text{-}3LE(A)}{}^{c}$	$k_{1CT \to 3LE(A)}{}^{d}$
		[cm^{-1}]	[eV]	[eV]	10^7 [s^{-1}]
H	ZNX	0.63	0.17	-0.09	6.69
diCl		0.49	0.16	-0.13	6.45
diBr		0.59	0.22	-0.11	4.27
H	PMMA	0.63	0.17	-0.05	3.41
diCl		0.49	0.16	-0.07	3.12
diBr		0.59	0.22	-0.06	1.98

^{a} - SOC constant value for the $^1CT \to {}^3LE(A)$ transition calculated in optimized ^1CT – state geometry;

^{b} - inner reorganization energy for $^1CT \to {}^3LE(A)$ transition ($\lambda_{out} = 0.05$ eV);

^{c} - energy gap from **Table 1**;

^{d} -predicted constant rate calculated using equation (S12).

Table S8. Computational data for prediction ^{1}CT $\to$ ^{3}LE(D) transition.

^{1}CT $\to$ ^{3}LE(D) Mean ^{1}CT values									
		^{1}CT		^{3}LE(D)		$V_{1CT\to3LE(D)}{}^{d}$	$\lambda_{1CT\to3LE(D)}{}^{e}$	$\Delta E_{1CT\text{-}3LE(D)}{}^{f}$	$k_{1CT\to3LE(D)}{}^{i}$
		[nm]^a	[eV]^b	[nm]^c	[eV]^b	[cm^{-1}]	[eV]	[eV]	10^7 [s^{-1}]
H	ZNX	423	2.93	392	3.16	0.70	0.23	0.23	0.016
diCl		418	2.97	410	3.02	1.20	0.24	0.06	0.880
diBr		421	2.95	412	3.01	3.30	0.28	0.06	6.122
H	PMMA	430	2.88	392	3.16	0.70	0.23	0.28	0.0003
diCl		437	2.90	410	3.02	1.20	0.24	0.12	0.177
diBr		428	2.89	412	3.01	3.30	0.28	0.11	1.810

^{1}CT $\to$ ^{3}LE(D) Rotameric ^{1}CT species in PMMA									
		^{1}CT		^{3}LE(D)		$V_{1CT\to3LE(D)}{}^{d}$	$\lambda_{1CT\to3LE(D)}{}^{e}$	$\Delta E_{1CT\text{-}3LE(D)}{}^{f}$	$k_{1CT\to3LE(D)}{}^{h}$
		[nm]^g	[eV]^b	[nm]^c	[eV]^b	[cm^{-1}]	[eV]	[eV]	10^7 [s^{-1}]
		high energy ^{1}CT species							
H	PMMA	419	2.96	392	3.16	0.70	0.23	0.20	0.005
diCl		415	2.99	410	3.02	1.20	0.24	0.03	1.542
diBr		416	2.99	412	3.01	3.30	0.28	0.02	15.33
		low energy ^{1}CT species							
H	PMMA	442	2.80	392	3.16	0.70	0.23	0.36	0.0001
diCl		439	2.83	410	3.02	1.20	0.24	0.20	0.016
diBr		440	2.82	412	3.01	3.30	0.28	0.19	0.173

^{a} - experimentally determined from steady-state PL spectra. **Figure S6**;

^{b} - energies calculated from relation: $E = 1240/\lambda_{onset}$;

^{c} - experimentally determined from phosphorescence spectra of donor fragments (**Figures S6H**);

^{d} - SOC values for the ^{1}CT $\to$ ^{3}LE(D) transition calculated for the optimized ^{1}CT-state geometry;

^{e} - inner reorganization energy for ^{1}CT $\to$ ^{3}LE(D) transition, $\lambda_{out} = 0.05$ eV;

^{f} - energy gap determined from the difference of respective onsets of PL spectra: $\Delta E_{1\text{-}2} = (1240/\lambda_{onset1} - 1240/\lambda_{onset2})$;

^{g} - determined from time-dependend PL spectra (see **Figure S11** and **Table S2**);

^{h} - predicted constant rates calculated from equation (S12).

**Table S9**. Summary of predicted ISC constant rates.

cmpd		Theoretical					Experimental
		$k_{1CT\rightarrow3LE(A)}$	$\mu_{1CT\rightarrow3LE(A)}$[a]	$k_{1CT\rightarrow3LE(D)}$	$\mu_{1CT\rightarrow3LE(D)}$[a]	$k_{1CT\rightarrow3LE(A)} + k_{1CT\rightarrow3LE(D)}$	k_{ISC}
		10^7 [s^{-1}]	[%]	10^7 [s^{-1}]	[%]	10^7 [s^{-1}]	10^7 [s^{-1}]
H	ZNX	6.69	100	0.016	0	6.7	5.1
diCl		6.45	88	0.880	12	7.3	6.1
diBr		4.27	41	6.122	59	10.4	38.5
H	PMMA	3.41	100	0.0003	0	3.4	3.8
diCl		3.12	95	0.177	5	3.3	4.1
diBr		1.98	52	1.810	48	3.5	30.8
		high energy ^{1}CT species					
H	PMMA	9.19	100	0.005	0	9.2	3.8
diCl		7.61	83	1.542	17	9.1	4.1
diBr		6.44	30	15.33	70	21.8	30.8
		low energy ^{1}CT species					
H	PMMA	0.80	100	0.0001	0	0.8	3.8
diCl		0.84	99	0.016	1	0.8	4.1
diBr		0.52	75	0.173	25	0.7	30.8

[a] - Relative contributions for respective transitions calculated as follows: $\mu_{1CT\rightarrow3LE(A)} = 100\% \cdot k_{1CT\rightarrow3LE(A)} / (k_{1CT\rightarrow3LE(A)} + k_{1CT\rightarrow3LE(D)})$ and $\mu_{1CT\rightarrow3LE(D)} = 100\% \cdot k_{1CT\rightarrow3LE(D)} / (k_{1CT\rightarrow3LE(A)} + k_{1CT\rightarrow3LE(D)})$

Calculations for rISC rate constants. rISC constant rates were calculated using Marcus-Hush formula (S12), computationally predicted λ values and experimentally determined ΔE_{ST} values. Due to the coexistence of excited molecules in various triplet states, their contribution to the rISC transition was considered as proportional to the population of respective triplet states (**Table S10**).

Determination of population of lowest triplet excited states
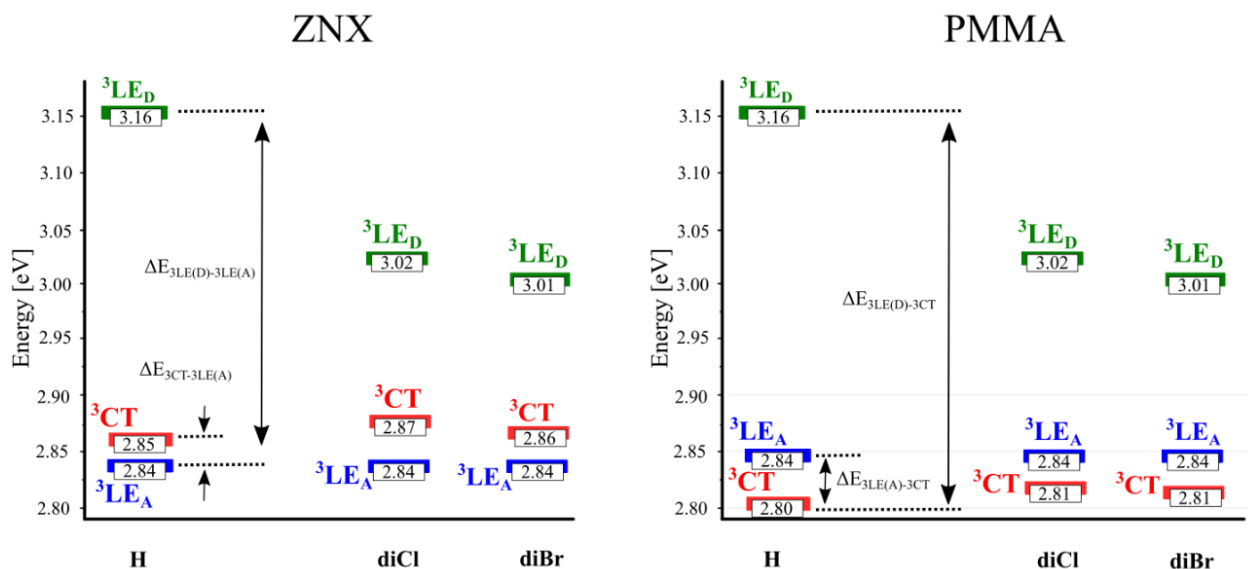
Figure S16. Alignment of the excited triplet states of investigated emitters.

Relative population χ_i of lowest triplet excited states was determinated using Boltzmann distribution law:

$$\chi_i = \frac{\exp\left(-\frac{\Delta E_i}{k_B T}\right)}{\sum_{i=1}^{N} \exp\left(-\frac{\Delta E_i}{k_B T}\right)}, \tag{S22}$$

where ΔE_i denotes the energy difference between lowest triplet state (T_1) and respective triplet state (T_i):

$$\Delta E_i = (T_i - T_1), \tag{S23}$$

$$a_i = \exp\left(-\frac{(T_i - T_1)}{k_B T}\right). \tag{S24}$$

Table S10. Population of lowest triplet excited states of emitters in ZNX and PMMA.

				ZNX					$\chi_{3LE(A)}$ [%]	χ_{3CT} [%]	$\chi_{3LE(D)}$ [%]
Alignment of triplet excited states:				$T_3 = {}^3$**LE(D)** $T_2 = {}^3$**CT** $T_1 = {}^3$**LE(A)**					^{3}**LE(A)**	^{3}**CT**	^{3}**LE(D)**
	T_1 [eV]	T_2 [eV]	T_3 [eV]	ΔE_{T2-T1} [eV]	ΔE_{T3-T1} [eV]	a_1	a_2	a_3	$\chi_{3LE(A)}$ [%]	χ_{3CT} [%]	$\chi_{3LE(D)}$ [%]
H	2.84	2.85	3.16	0.01	0.32	1	0.55	<0.0001	64.6	35.4	<0.001
diCl	2.84	2.87	3.02	0.03	0.18	1	0.35	0.00061	74.0	25.9	0.045
diBr	2.84	2.86	3.01	0.02	0.17	1	0.43	0.00092	69.6	30.3	0.064

				PMMA					χ_{3CT} [%]	$\chi_{3LE(A)}$ [%]	$\chi_{3LE(D)}$ [%]
Alignment of triplet excited states:				$T_3 = {}^3$**LE(D)** $T_2 = {}^3$**LE(A)** $T_1 = {}^3$**CT**					^{3}**CT**	^{3}**LE(A)**	^{3}**LE(D)**
	T_1 [eV]	T_2 [eV]	T_3 [eV]	ΔE_{T2-T1} [eV]	ΔE_{T3-T1} [eV]	a_1	a_2	a_3	χ_{3CT} [%]	$\chi_{3LE(A)}$ [%]	$\chi_{3LE(D)}$ [%]
H	2.80	2.84	3.16	0.04	0.36	1	0.23	<0.001	81.7	18.3	<0.001
diCl	2.81	2.84	3.02	0.03	0.21	1	0.36	0.0002	73.1	26.9	0.017
diBr	2.81	2.84	3.01	0.03	0.20	1	0.36	0.0003	73.1	26.9	0.029

Table S11. Computational data for rISC constant rate prediction within ^{3}LE(A)→^{1}CT and ^{3}LE(D)→^{1}CT transitions.

^{3}LE(A) → ^{1}CT

		$V_{3LE(A)\to1CT}{}^a$ [cm^{-1}]	$\lambda_{3LE(A)\to1CT}{}^b$ [eV]	$\Delta E_{3LE(A)-1CT}{}^c$ [eV]	$\chi_{3LE(A)}{}^d$ [%]	$k_{3LE(A)\to1CT}{}^e$ [s^{-1}]	$\chi_{3LE(A)}k_{3LE(A)\to1CT}{}^f$ [s^{-1}]
H	ZNX	0.24	0.17	0.09	64	3.2 x 10^5	2.0 x 10^5
diCl		0.51	0.16	0.13	74	5.2 x 10^5	3.9 x 10^5
diBr		0.24	0.22	0.11	69	1.3 x 10^5	8.3 x 10^4
H	PMMA	0.24	0.17	0.05	18	1.1 x 10^6	1.9 x 10^5
diCl		0.51	0.16	0.07	27	3.8 x 10^6	1.0 x 10^6
diBr		0.24	0.22	0.06	27	4.8 x 10^5	1.3 x 10^5

^{3}LE(D) → ^{1}CT

		$V_{3LE(D)\to1CT}{}^a$ [cm^{-1}]	$\lambda_{3LE(D)\to1CT}{}^b$ [eV]	$\Delta E_{3LE(D)-1CT}{}^c$ [eV]	$\chi_{3LE(D)}{}^d$ [%]	$k_{3LE(D)\to1CT}{}^e$ [s^{-1}]	$\chi_{3LE(D)}k_{3LE(D)\to1CT}{}^f$ [s^{-1}]
H	ZNX	0.70	0.23	0.23	0.01	1.6 x 10^4	1.6 x 10^0
diCl		1.21	0.24	0.05	0.05	8.9 x 10^6	4.5 x 10^3
diBr		3.10	0.28	0.06	0.10	5.4 x 10^7	5.4 x 10^4
H	PMMA	0.70	0.23	0.28	0.01	3.2 x 10^3	3.2 x 10^{-1}
diCl		1.21	0.24	0.12	0.02	1.8 x 10^6	3.6 x 10^2
diBr		3.10	0.28	0.11	0.03	1.6 x 10^7	4.8 x 10^3

^{a} - SOC values for the ^{3}LE(A) → ^{1}CT transition calculated in optimized ^{3}LE(A) – state geometry and for ^{3}LE(D) → ^{1}CT transition calculated in optimized ^{3}LE(D) – state geometry, respectively;
^{b} - reorganization energies for the ^{3}LE(A) → ^{1}CT and ^{3}LE(D) → ^{1}CT transitions, respectively;
^{c} - energy gap between ^{3}LE(A), ^{3}LE(D) and ^{1}CT states (see **Table S1**);
^{d} - estimated population of ^{3}LE(A) and ^{3}LE(D) triplet states (see **Table S10**);
^{e} - calculated rISC rate constant using equation (S12);
^{f} - calculated rISC constant rates corrected on population of respective excited triplet states.

Section S6: Computational details for the prediction of rISC rate constant within rotational model via direct ^{3}CT-^{1}CT transition

Within the rotational model, the total $k_{3CT \rightarrow 1CT}$ consists of fractional rate constant $k_{3CT \rightarrow 1CT}[\theta_i]$, originating from various θ-rotamers (as depicted in **Figures 1B** and **1F**):

$$k_{3CT \rightarrow 1CT} = \sum_{i=1}^{n} p[\theta_i] \cdot k_{3CT \rightarrow 1CT}[\theta_i] \tag{S25}$$

where:

- $p[\theta_i]$ - molar fraction of i-th rotamer with θ dihedral angle between donor and acceptor (**Figure 1B**) within Boltzmann distribution function,

- n is the number of considered rotamers;

- $k_{3CT \rightarrow 1CT}[\theta_i]$ - fractional rate constant, calculated using Marcus-Hush equation as follows:

$$k_{3CT \rightarrow 1CT}[\theta_i] = \frac{(V_{3CT \rightarrow 1CT}[\theta_i])^2}{\hbar} \sqrt{\frac{\pi}{k_B T \, \lambda_{3CT \rightarrow 1CT}[\theta_i]}} \exp\left[-\frac{(\Delta E_{3CT-1CT}[\theta_i] + \lambda_{3CT \rightarrow 1CT}[\theta_i])^2}{4 k_B T \lambda_{3CT \rightarrow 1CT}[\theta_i]}\right], \tag{S26}$$

where:

- $V_{3CT \rightarrow 1CT}[\theta_i]$ - SOC constant calculated for i-th rotamer with θ dihedral angle at the ^{3}CT-state geometry,

- $\lambda_{3CT \rightarrow 1CT}[\theta_i]$ - reorganization energy,

- $\Delta E_{3CT-1CT}[\theta_i]$ - energy gap between ^{1}CT and ^{3}CT states of i-th rotamer with θ dihedral angle,

- k_B is Boltzmann constant ($k_B = 8.617 \times 10^{-5}$ eV/K),

- T - temperature (for all of calculations T = 298 K).

Reorganization energy $\lambda_{3CT \rightarrow 1CT}[\theta_i]$ consists of two terms (inner $\lambda_{3CT \rightarrow 1CT}^{in}[\theta_i]$ and outer $\lambda_{3CT \rightarrow 1CT}^{out}$):

$$\lambda_{3CT \rightarrow 1CT}[\theta_i] = \lambda_{3CT \rightarrow 1CT}^{in}[\theta_i] + \lambda_{3CT \rightarrow 1CT}^{out}. \tag{S27}$$

The first term $\lambda_{3CT \rightarrow 1CT}^{in}[\theta_i]$ refers to the energy that is dissipated by molecule during relaxation to the equilibrium geometry in a given state.

It can be calculated using the formula:

$$\lambda_{3CT \to 1CT}^{in}[\theta_i] = E_{3CT}^{1CT}[\theta_i] - E_{1CT}^{1CT}, \qquad (S28)$$

where:

- $E_{3CT}^{1CT}[\theta_i]$ - TD-DFT energy of ^{1}CT state at ^{3}CT-state geometry calculated for i-th rotamer with θ dihedral angle,

- E_{1CT}^{1CT} – TD-DFT energy of ^{1}CT state at optimized ^{1}CT-state geometry.

The second term $\lambda_{3CT \to 1CT}^{out}$ is a measure of solvatation effects, and in case of interaction between excited states with the same nature (CT) it can be approximated as follows:

$$\lambda_{3CT \to 1CT}^{out} \approx \Delta E_{3CT-1CT}[\theta_i]. \qquad (S29)$$

Boltzmann distribution law was used to estimate relative population of rotamers $p[\theta_i]$:

$$p[\theta_i] = Z^{-1} \cdot \exp\left(-\frac{\Delta E[\theta_i]}{k_B T}\right), \qquad (S30)$$

$$\Delta E[\theta_i] = E[\theta_i] - E_{1CT}^{1CT}, \qquad (S31)$$

$$Z = \sum_{i=1}^{n} \exp\left(-\frac{\Delta E[\theta_i]}{k_B T}\right), \qquad (S32)$$

where:

- $E[\theta_i]$ – energy calculated for i-th rotamer with θ dihedral angle,

- E_{1CT}^{1CT} - energy at optimized ^{1}CT- state geometry.

Below, complete set of computed parameters for prediction of $k_{3CT \to 1CT}$ in **H**, **diCl** and **diBr** within developed rotational model is presented (**Tables S12** – **S14** and **Figures S17** – **S19**).

Table S12. Computational parameters for $k_{3CT\rightarrow1CT}$ prediction in **H** using rotational model.

			Computational parameters for the prediction of $k_{3CT\rightarrow1CT}$ in **H**				
θ_i	$\Delta E[\theta_i]$	$p[\theta_i]$	$\Delta E_{3CT-1CT}[\theta_i]$	$V_{3CT\rightarrow1CT}[\theta_i]$	$\lambda_{3CT\rightarrow1CT}[\theta_i]$	$k_{3CT\rightarrow1CT}[\theta_i]$	$p[\theta_i]\cdot k_{3CT\rightarrow1CT}[\theta_i]$
[^{O}]	[meV]	[%]	[meV]	[cm^{-1}]	[meV]	10^4 [s^{-1}]	10^4 [s^{-1}]
90	0.0	4.1	4.7	0	0.0	0.0	0.000
89	0.2	4.1	4.8	0.01	0.3	0.1	0.004
88	0.5	4.0	5.5	0.02	1.3	0.3	0.025
87	1.0	3.9	6.6	0.03	3.0	1.5	0.057
86	1.7	3.8	8.3	0.04	5.3	2.5	0.095
85	2.6	3.7	10.4	0.05	8.4	2.9	0.134
84	3.9	3.5	13.1	0.05	12.3	4.7	0.125
83	5.5	3.3	16.2	0.06	16.9	4.9	0.159
82	7.4	3.1	19.6	0.06	22.3	5.0	0.112
81	9.6	2.8	23.7	0.07	28.5	5.5	0.119
80	12.1	2.6	28.1	0.08	35.4	5.8	0.118
79	14.9	2.3	33.1	0.09	43.1	5.9	0.110
78	18.1	2.0	38.3	0.10	51.6	5.8	0.096
77	21.7	1.8	44.0	0.11	60.8	5.4	0.080
76	25.7	1.5	50.2	0.12	70.9	4.2	0.063
75	30.2	1.3	56.5	0.13	81.7	3.8	0.048
74	35.1	1.0	63.3	0.14	93.4	3.3	0.034
73	40.5	0.8	70.5	0.15	105.9	2.8	0.024
72	46.5	0.7	77.9	0.16	119.2	2.1	0.016
71	52.9	0.5	85.6	0.16	133.4	1.7	0.009
70	60.0	0.4	93.6	0.16	148.4	1.2	0.005
69	67.8	0.3	101.7	0.16	164.2	0.8	0.002
68	76.3	0.2	110.2	0.16	181.2	0.6	0.001
67	85.7	0.1	118.3	0.17	199.2	0.4	0.001
66	95.9	0.1	127.8	0.17	218.2	0.3	0.000
65	107.0	0.1	136.8	0.17	238.3	0.3	0.000
64	119.1	0.0	145.9	0.18	259.4	0.2	0.000
63	132.2	0.0	155.3	0.18	281.2	0.1	0.000
62	146.5	0.0	164.7	0.18	305.4	0.1	0.000
61	163.4	0.0	172.6	0.19	330.2	0.0	0.000
60	182.4	0.0	180.1	0.19	356.5	0.0	0.000

Rate constant calculated for **H** within rotational model	$k_{3CT\rightarrow1CT}$	=	**2.81** [10^4 s^{-1}]
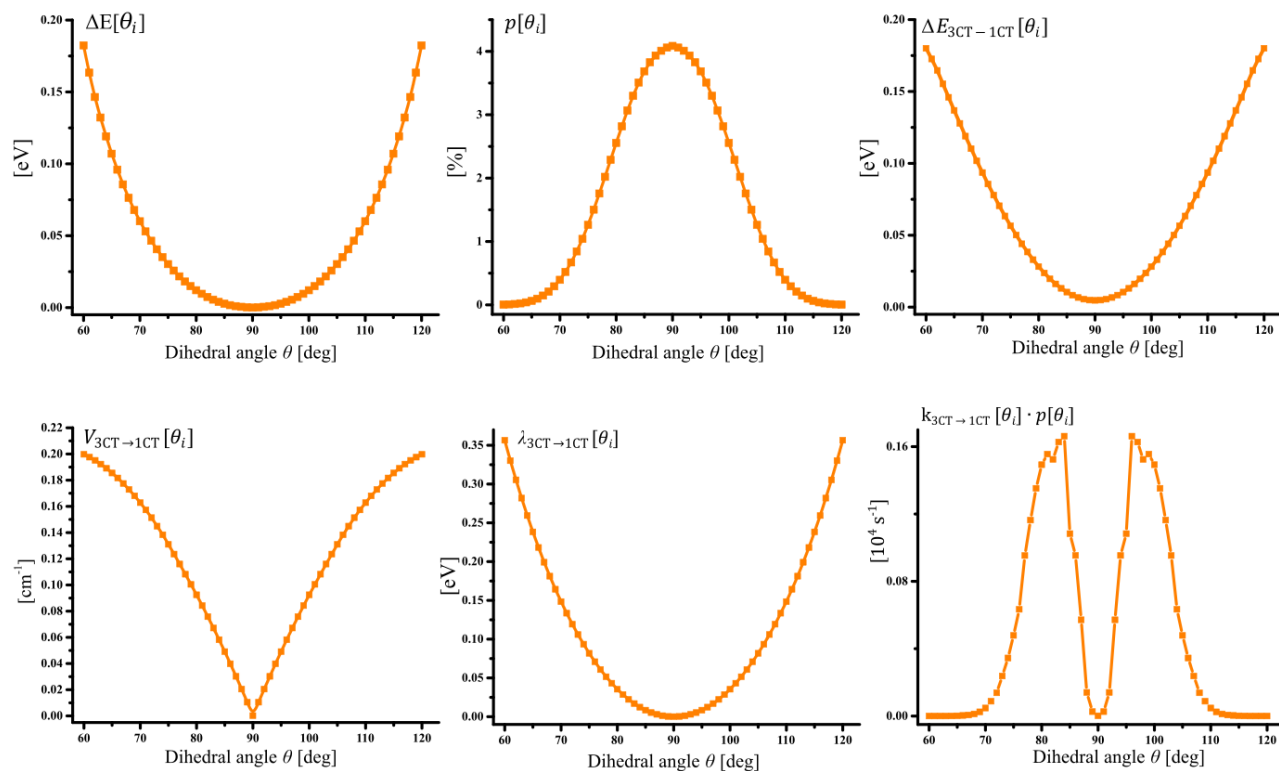
Figure S17. Computational parameters for the prediction of $k_{3CT\rightarrow1CT}$ in **H** calculated within rotational model.

			Computational parameters for prediction $k_{3CT\rightarrow1CT}$ in **diCl**				
θ_i	$\Delta E[\theta_i]$	$p[\theta_i]$	$\Delta E_{3CT-1CT}[\theta_i]$	$V_{3CT\rightarrow1CT}[\theta_i]$	$\lambda_{3CT\rightarrow1CT}[\theta_i]$	$k_{3CT\rightarrow1CT}[\theta_i]$	$p[\theta_i]\cdot k_{3CT\rightarrow1CT}[\theta_i]$
[°]	[meV]	[%]	[meV]	[cm⁻¹]	[meV]	10^4 [s⁻¹]	10^4 [s⁻¹]
90	0.0	3.5	5.2	0.00	0.0	0.0	0.000
89	0.4	3.4	5.4	0.01	0.1	0.1	0.000
88	0.7	3.4	5.8	0.01	1.0	0.5	0.005
87	0.9	3.3	7.1	0.02	2.3	0.6	0.021
86	1.2	3.3	8.6	0.03	4.3	1.3	0.045
85	1.8	3.2	11.2	0.04	7.9	2.3	0.058
84	2.6	3.1	13.5	0.05	10.9	3.2	0.089
83	3.4	3.0	16.6	0.05	14.9	2.9	0.087
82	4.5	2.9	20.1	0.06	19.4	3.6	0.091
81	5.8	2.8	24.2	0.06	24.7	4.2	0.082
80	7.4	2.6	28.6	0.07	30.8	3.5	0.084
79	9.3	2.4	34.3	0.07	38.4	3.7	0.068
78	11.5	2.2	39.7	0.08	45.9	3.0	0.066
77	13.9	2.0	45.4	0.08	54.1	3.0	0.047
76	16.7	1.8	51.6	0.09	63.0	2.3	0.042
75	19.9	1.6	58.1	0.09	72.6	2.2	0.029
74	23.4	1.4	64.9	0.09	83.0	1.7	0.019
73	27.4	1.2	72.1	0.09	94.0	1.3	0.012
72	31.8	1.0	79.7	0.10	105.9	1.1	0.009
71	36.7	0.8	87.5	0.11	118.7	0.8	0.007
70	42.2	0.7	95.6	0.11	132.2	0.6	0.004
69	48.4	0.5	104.0	0.12	146.7	0.4	0.003
68	55.2	0.4	112.6	0.13	162.1	0.3	0.002
67	62.8	0.3	121.4	0.14	178.5	0.2	0.001
66	71.2	0.2	130.4	0.13	195.8	0.1	0.000
65	80.6	0.2	139.5	0.14	214.2	0.1	0.000
64	90.8	0.1	148.8	0.14	233.7	0.1	0.000
63	102.2	0.1	158.4	0.14	254.5	0.0	0.000
62	114.7	0.0	167.8	0.15	276.4	0.0	0.000
61	128.5	0.0	177.7	0.15	299.8	0.0	0.000
60	143.8	0.0	187.4	0.16	324.8	0.0	0.000

Rate constant calculated for **diCl** within rotational model $\quad k_{3CT\rightarrow1CT} \quad = \quad$ **1.75** $[10^4\ \text{s}^{-1}]$
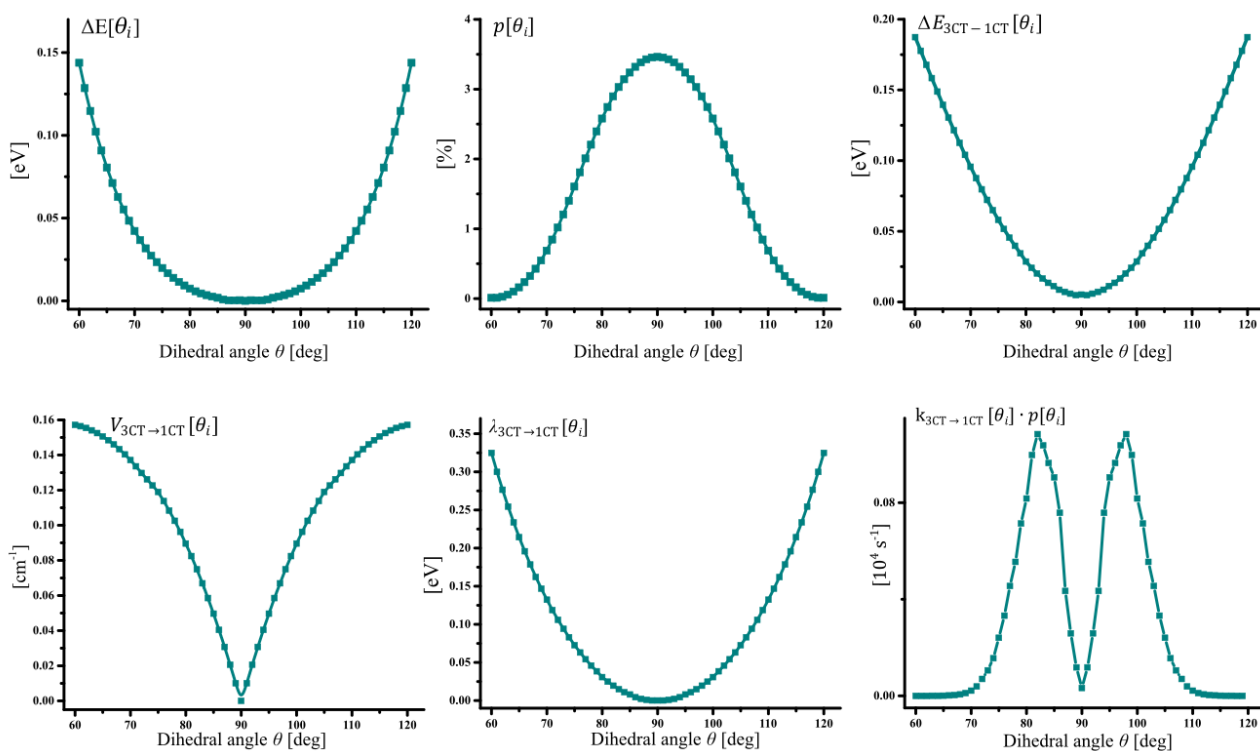
Figure S18. Computational parameters for prediction $k_{3CT\rightarrow1CT}$ in **diCl** calculated within rotational model.

Table S14 Computational parameters for $k_{3CT \to 1CT}$ prediction in **diBr** using rotational model.

	Computational parameters for the prediction of $k_{3CT \to 1CT}$ in **diBr**						
θ_i	$\Delta E[\theta_i]$	$p[\theta_i]$	$\Delta E_{3CT-1CT}[\theta_i]$	$V_{3CT \to 1CT}[\theta_i]$	$\lambda_{3CT \to 1CT}[\theta_i]$	$k_{3CT \to 1CT}[\theta_i]$	$p[\theta_i] \cdot k_{3CT \to 1CT}[\theta_i]$
[°]	[meV]	[%]	[meV]	[cm⁻¹]	[meV]	10^4 [s⁻¹]	10^4 [s⁻¹]
90	0.0	3.4	4.8	0.00	0.00	0.00	0.000
89	0.0	3.4	5.1	0.01	0.00	0.01	0.009
88	0.1	3.4	5.8	0.01	0.00	0.27	0.030
87	0.2	3.3	6.9	0.02	0.00	0.87	0.043
86	0.4	3.3	8.5	0.02	0.00	1.26	0.039
85	0.9	3.3	10.8	0.03	0.01	1.18	0.049
84	1.6	3.2	13.1	0.03	0.01	1.50	0.058
83	2.7	3.1	16.1	0.04	0.01	1.86	0.056
82	4.0	2.9	19.5	0.04	0.02	1.89	0.047
81	5.5	2.8	23.4	0.05	0.02	1.70	0.041
80	7.3	2.6	27.7	0.05	0.03	1.57	0.037
79	9.3	2.4	32.4	0.06	0.04	1.54	0.028
78	11.6	2.2	37.5	0.06	0.04	1.26	0.029
77	14.1	2.0	43.0	0.07	0.05	1.45	0.020
76	16.9	1.8	48.9	0.07	0.06	1.15	0.014
75	20.1	1.6	55.1	0.08	0.07	0.89	0.013
74	23.5	1.4	61.7	0.08	0.08	0.93	0.008
73	27.5	1.2	68.6	0.08	0.09	0.70	0.007
72	32.1	1.0	75.7	0.09	0.10	0.68	0.004
71	37.3	0.8	83.2	0.09	0.12	0.50	0.002
70	43.1	0.6	91.0	0.09	0.13	0.36	0.002
69	49.6	0.5	98.5	0.10	0.14	0.33	0.001
68	56.7	0.4	106.7	0.10	0.16	0.24	0.001
67	64.5	0.3	115.2	0.10	0.17	0.20	0.000
66	73.1	0.2	123.7	0.11	0.19	0.17	0.000
65	82.5	0.1	132.5	0.11	0.21	0.12	0.000
64	92.9	0.1	141.4	0.11	0.23	0.08	0.000
63	104.4	0.1	150.4	0.11	0.25	0.06	0.000
62	117.0	0.0	159.6	0.11	0.27	0.04	0.000
61	130.8	0.0	168.8	0.12	0.29	0.03	0.000
60	143.1	0.0	181.2	0.12	0.32	0.02	0.000

Rate constant calculated for **diBr** within rotational model $\quad k_{3CT \to 1CT} \quad = \quad$ **1.08** $[10^4\ \text{s}^{-1}]$
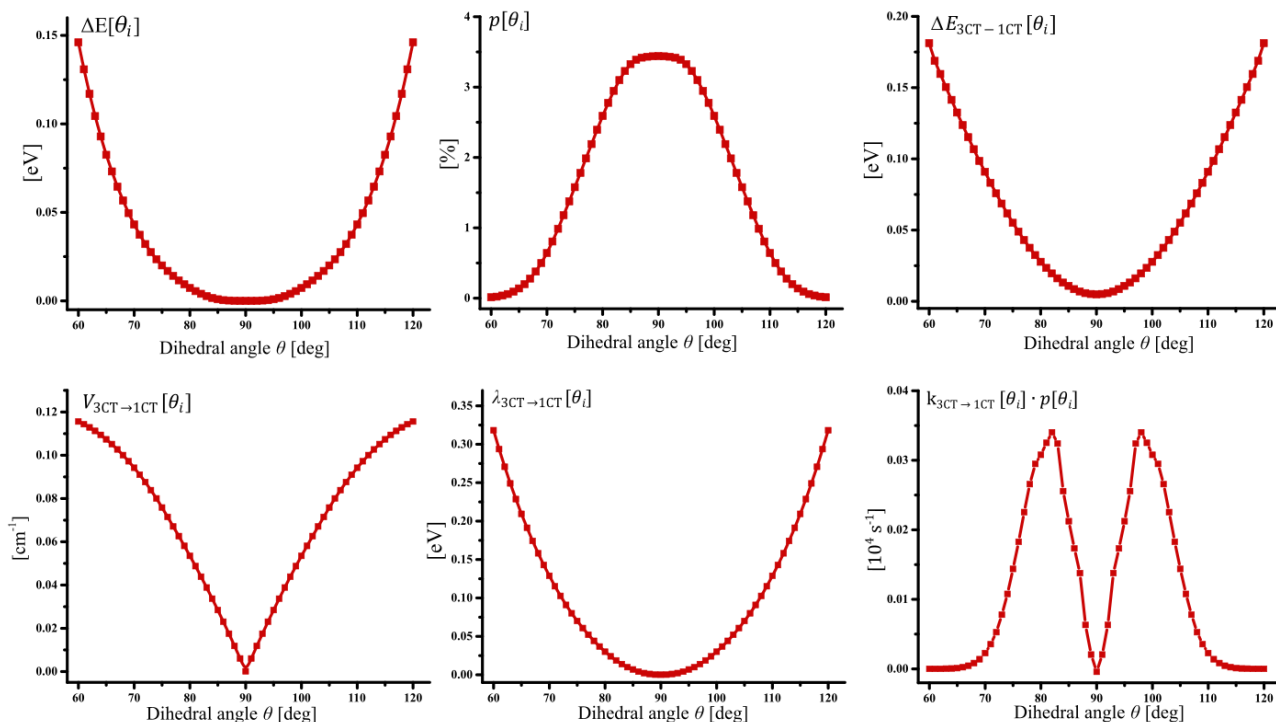
Figure S19. Computational parameters for the prediction of $k_{3CT \to 1CT}$ in **diBr** calculated within rotational model.

The statistically weighted oscillator strengths (f) values for all rotamers were calculated according to the procedure reported previously.[S3] Thus obtained f value slightly increases with the introduction of halogen from 0.016 (**H**) to 0.020 (**diCl** and **diBr**). One can thus suggest that the value of oscillator strength reversely correlates with the CT strength.

Section S7: Computational details for the prediction of rISC rate constant within the vibrational model via direct ^{3}CT-^{1}CT transition

Within the vibrationally-assisted direct SOC model presented below, total $k_{3CT \to 1CT}$ consists of fractional constant rates $k_{3CT \to 1CT}^{\omega_i}$, originating from one θ-rotamer ($\theta = 90°$) at various deviations from optimal geometry induced by low-frequency vibrations (<100 cm^{-1}):

$$k_{3CT \to 1CT} = \sum_{i=1}^{n} k_{3CT \to 1CT}^{\omega_i} \tag{S33}$$

where ω_i is i-th vibrational mode, n is the number of considered modes (here $n = 8$, see **Figure S19**).
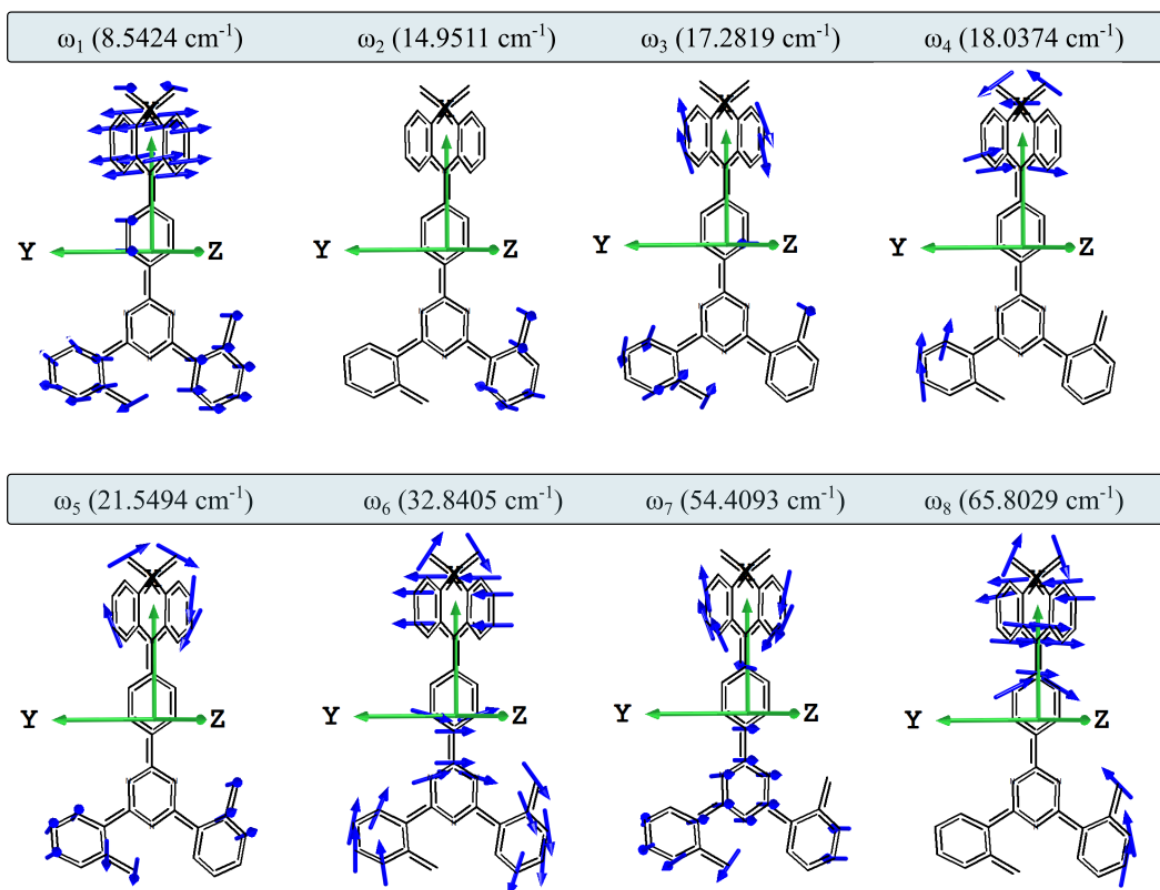
Figure S20. Vibrational modes of **H** calculated in S_0-state geometry with displacement vectors shown.

Single point TD-DFT calculations of energetic and SOC parameters were performed for various modifications of the S_0-state 90-rotamer structure, in which each vibration was "scanned" by changing its amplitude A in a $-2 - +2$ range. Such structures were generated using Chemchraft software, version 1.8. For the i vibrational mode, fractional constant rate $k_{3CT \to 1CT}^{\omega_i}$ was performed taking into account contribution of each vibrational isomer as follows:

$$k_{3CT \to 1CT}^{\omega_i} = \sum_{j=1}^{m} k_{\omega_i}[A_j] \cdot p_{\omega_i}[A_j],$$

(S34)

where:

- $p_{\omega_i}[A_j]$ - Boltzmann distribution function, molar fraction of j-th isomer with A_j amplitude in the ω_i vibration,

- m - number of calculated isomers, usually $m = 29$ unless mentioned differently.

- $k_{\omega_i}[A_j]$ – the ^{3}CT-^{1}CT transition rate constant calculated for the j-th vibrational isomer using Marcus-Hush equation:

$$k_{\omega_i}[A_j] = \frac{(V_{3CT \to 1CT}[A_j])^2}{\hbar} \sqrt{\frac{\pi}{k_B T \lambda_{3CT \to 1CT}[A_j]}} \exp\left[-\frac{(\Delta E_{3CT-1CT}[A_j] + \lambda_{3CT \to 1CT}[A_j])^2}{4 k_B T \lambda_{3CT \to 1CT}[A_j]}\right],$$

(S35)

where:

- $V_{3CT \to 1CT}[A_j]$ – SOC constant of the j-th isomer at the ^{3}CT-state geometry,

- $\lambda_{3CT \to 1CT}[A_j]$ – reorganization energy of the j-th isomer at the ^{3}CT-state geometry,

- $\Delta E_{3CT-1CT}[A_j]$ – energy gap between ^{1}CT and ^{3}CT states in j-th isomer,

- k_B is Boltzmann constant ($k_B = 8.617 \times 10^{-5}$ eV/K),

- T – temperature, for all calculations T = 298 K.

Reorganization energy consists of two terms (inner and outer):

$$\lambda_{3CT \to 1CT}[A_j] = \lambda_{3CT \to 1CT}^{in}[A_j] + \lambda_{3CT \to 1CT}^{out}$$

(S36)

The first term $\lambda_{3CT \to 1CT}^{in}[A_j]$ refers to the energy that is dissipated by the molecule relaxing to the equilibrium geometry at given state. It can be calculated using the formula:

$$\lambda^{in}_{3CT \to 1CT}[A_j] = E^{1CT}_{3CT,\omega_i}[A_j] - E^{1CT}_{1CT,\omega_i}[A_0],$$ (S37)

where:

- $E^{1CT}_{3CT,\omega_i}[A_j]$ — TD-DFT energy of ^1CT state at ^3CT-state geometry calculated for j-th isomer within ω_i vibration,

- $E^{1CT}_{1CT,\omega_i}[A_0]$ — TD-DFT energy of ^1CT state at optimized (A_0 refers to amplitude = 0) ^1CT-state geometry calculated within ω_i vibration.

The second term $\lambda^{out}_{3CT \to 1CT}$ is a measure of solvatation effects, and in case of interaction between excited states with the same nature (CT) can be approximated as follows:

$$\lambda^{out}_{3CT \to 1CT} \approx \Delta E_{3CT-1CT}[A_j].$$ (S38)

Boltzmann distribution law was used to estimate relative population of isomers ($p_{\omega_i}[A_j]$), which was calculated for the ground S_0-state:

$$p_{\omega_i}[A_j] = Z^{-1} \cdot \exp\left(-\frac{\Delta E_{\omega_i}[A_j]}{k_B T}\right)$$ (S39)

$$\Delta E_{\omega_i}[A_j] = E_{\omega_i}[A_j] - E[A_0]$$ (S40)

$$Z = \sum_{j=1}^{m} \exp\left(-\frac{\Delta E_{\omega_i}[A_j]}{k_B T}\right)$$ (S41)

$E_{\omega_i}[A_j]$ – energy calculated for j-th isomer within the ω_i vibration at S_0 state,

$E[A_0]$ - energy at the S_0-state optimized geometry.

At the end, contribution of the ^3CT-^1CT transition rate constant from each vibrational mode $\mu^{\omega_i}_{3CT \to 1CT}$ to the total $k_{3CT \to 1CT}$ was calculated (see **Table S18**) using:

$$\mu^{\omega_i}_{3CT \to 1CT} = \frac{k^{\omega_i}_{3CT \to 1CT}}{\sum_{i=1}^{n=8} k^{\omega_i}_{3CT \to 1CT}}.$$ (S42)

As an example, below we present a complete set of computed parameters for the prediction of the ^{3}CT-^{1}CT transition rate constant within the first vibrational mode ($k^{\omega_1}_{3CT\rightarrow1CT}$) in **H**, **diCl** and **diBr** (**Tables S15 – S17** and **Figures S20 – S24**).

Table S15. Computational parameters for the prediction of $k_{3CT \to 1CT}^{\omega_1}$ in **H**.

A_j	$\Delta E_{\omega_1}[A_j]$	$p_{\omega_1}[A_j]$	$\Delta E_{3CT-1CT}[A_j]$	$V_{3CT \to 1CT}[A_j]$	$\lambda_{3CT \to 1CT}[A_j]$	$k_{\omega_1}[A_j]$	$k_{\omega_1}[A_j] \cdot p_{\omega_1}[A_j]$
	[eV]	[%]	[meV]	[cm⁻¹]	[meV]	10^4 [s⁻¹]	10^4 [s⁻¹]
-2.00	0.0814	0.23	11.46	0.044	136.23	0.844	0.0019
-1.80	0.0624	0.48	10.18	0.040	107.72	1.041	0.0049
-1.50	0.0401	1.14	8.46	0.033	72.86	1.276	0.0146
-1.40	0.0339	1.45	7.95	0.031	63.15	1.325	0.0192
-1.20	0.0236	2.16	7.05	0.026	46.37	1.360	0.0294
-1.00	0.0155	2.96	6.23	0.022	32.71	1.301	0.0386
-0.80	0.0094	3.77	5.61	0.018	22.05	1.126	0.0429
-0.50	0.0032	4.78	4.90	0.011	10.99	0.707	0.0337
-0.40	0.0019	5.03	4.73	0.009	8.53	0.524	0.0269
-0.30	0.0010	5.22	4.57	0.007	6.62	0.340	0.0178
-0.25	0.0006	5.30	4.54	0006	5.93	0.251	0.0133
-0.20	0.0003	5.35	4.46	0.004	5.30	0.171	0.0091
-0.15	0.0001	5.39	4.44	0.003	4.87	0.102	0.0054
-0.10	0.0000	5.42	4.44	0.002	4.61	0.045	0.0025
0	0.0000	5.42	4.38	0.000	4.38	0.000	0.0000
0.10	0.0003	5.35	4.41	0.002	4.77	0.045	0.0025
0.15	0.0006	5.29	4.41	0.003	5.13	0.101	0.0053
0.20	0.0010	5.22	4.44	0.004	5.66	0.162	0.0088
0.25	0.0014	5.13	4.49	0.006	6.34	0.242	0.0124
0.30	0.0019	5.03	4.49	0.007	7.07	0.332	0.0165
0.40	0.0032	4.78	4.63	0.009	9.10	0.521	0.0243
0.50	0.0048	4.49	4.76	0.011	11.65	0.679	0.0308
0.80	0.0119	3.41	5.41	0.018	22.78	1.121	0.0381
1.00	0.0187	2.62	6.04	0.022	33.34	1.292	0.0337
1.20	0.0274	1.86	6.78	0.026	46.48	1.367	0.0254
1.40	0.0383	1.22	7.65	0.031	62.56	1.345	0.0164
1.50	0.0447	0.95	8.14	0.033	71.79	1.310	0.0123
1.80	0.0683	0.38	9.82	0.040	104.75	1.093	0.0041
2.00	0.0881	0.18	11.13	0.044	131.62	0.898	0.0016

Fractional rate constant calculated for **H** within ω_1 vibration: $k_{3CT \to 1CT}^{\omega_1}$ = **0.4923**
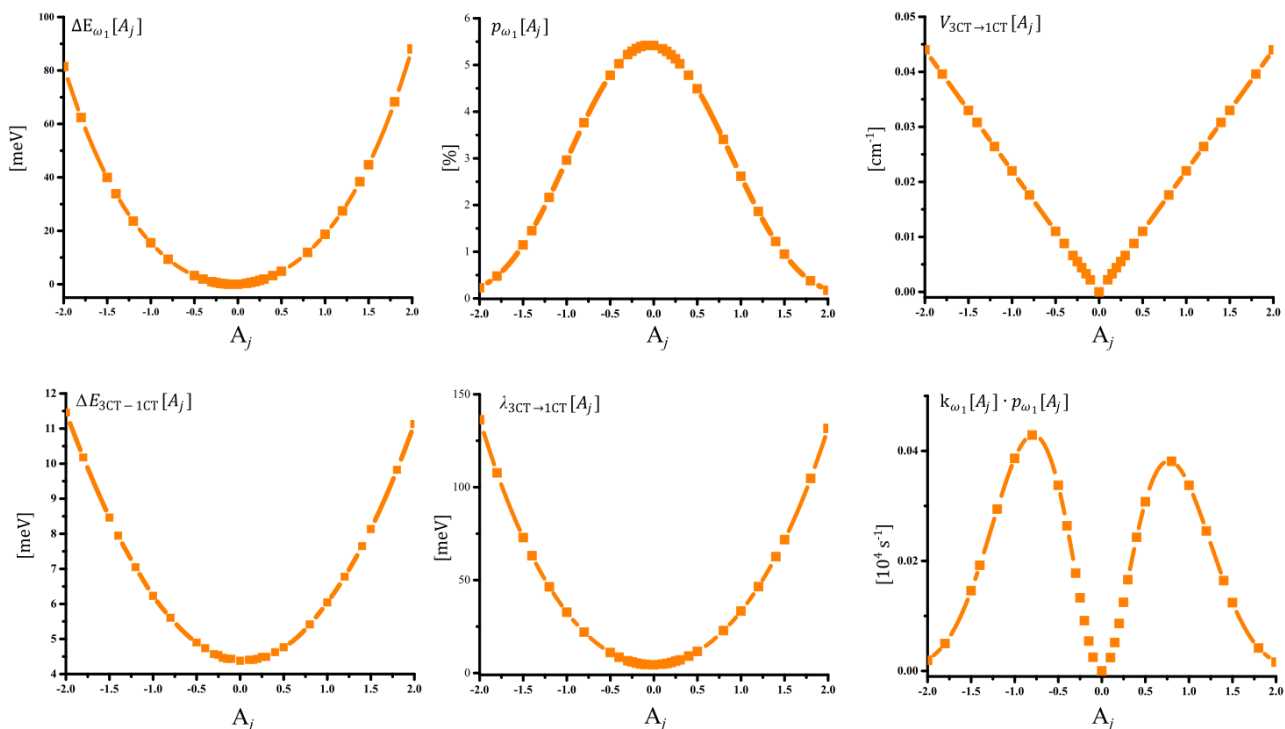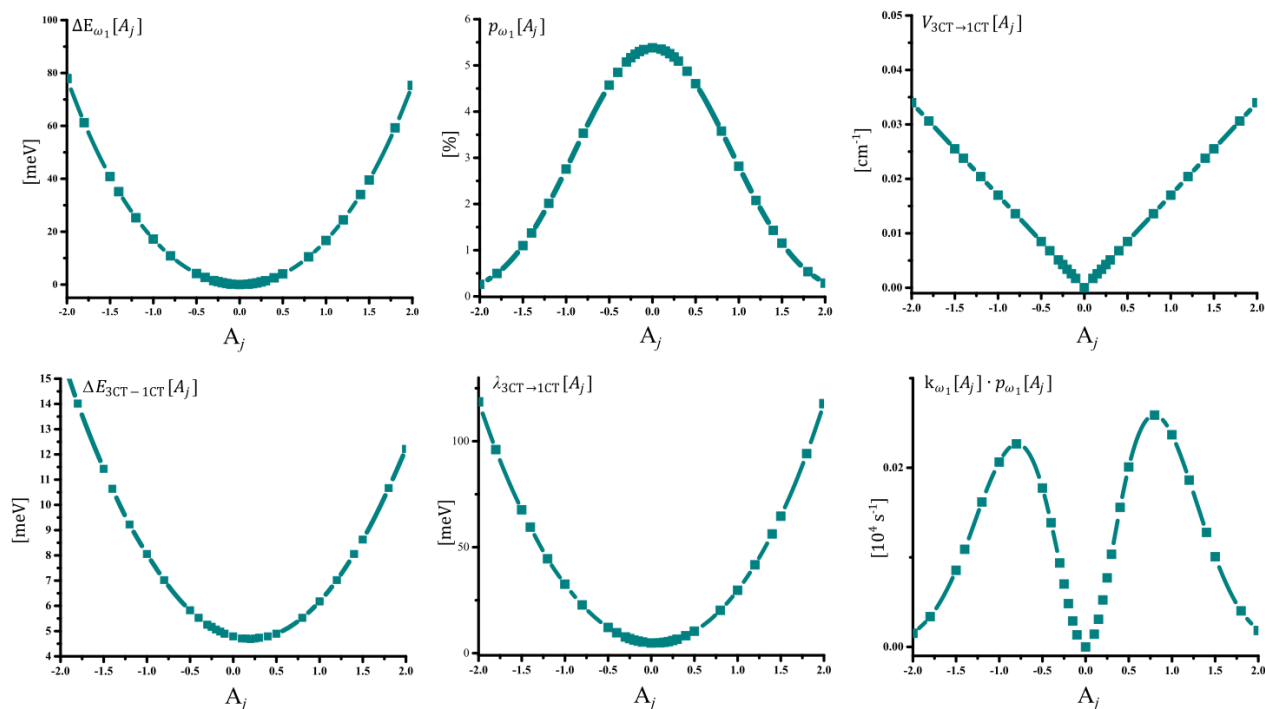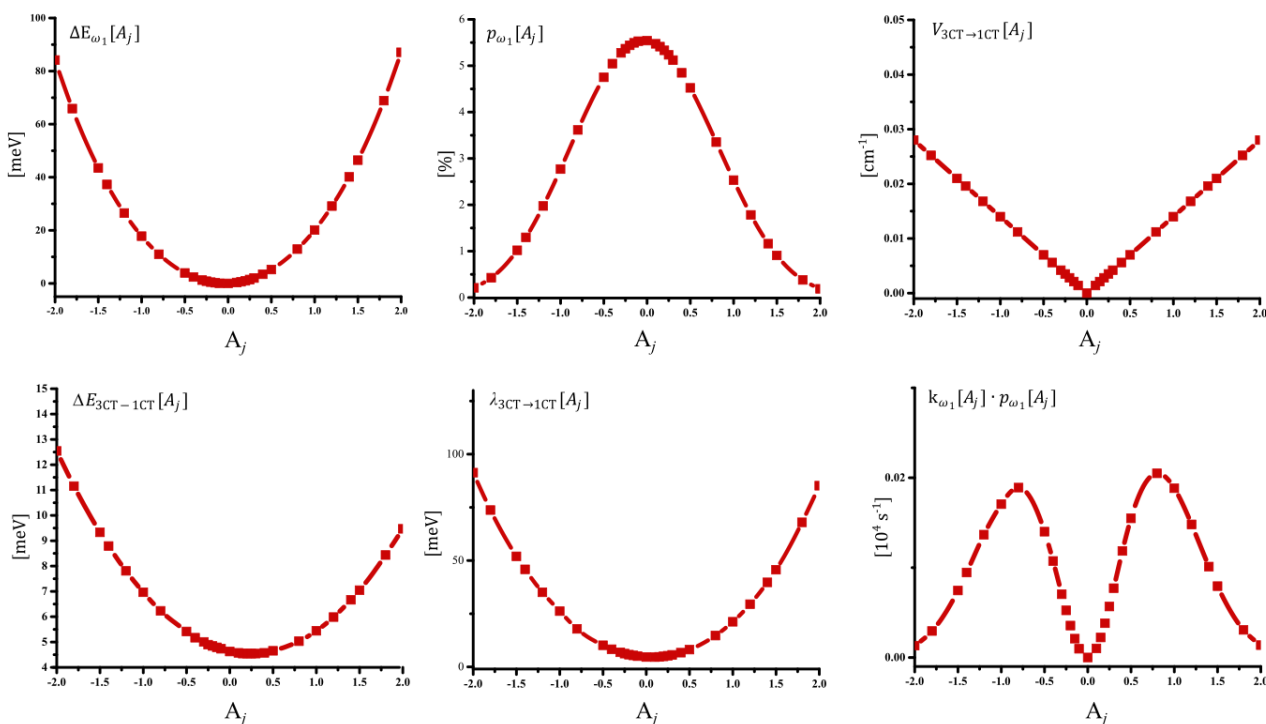

Figure S21. Computational parameters for the prediction of $k_{3CT \to 1CT}^{\omega_1}$ in **H**.

Table S16. Computational parameters for the prediction of $k^{\omega_1}_{3CT \to 1CT}$ in **diCl**.

	Computational parameters for the prediction of $k^{\omega_1}_{3CT \to 1CT}$ in **diCl**						
A_j	$\Delta E_{\omega_1}[A_j]$	$p_{\omega_1}[A_j]$	$\Delta E_{3CT-1CT}[A_j]$	$V_{3CT \to 1CT}[A_j]$	$\lambda_{3CT \to 1CT}[A_j]$	$k_{\omega_1}[A_j]$	$k_{\omega_1}[A_j] \cdot p_{\omega_1}[A_j]$
	[eV]	[%]	[meV]	[cm⁻¹]	[meV]	10^4 [s⁻¹]	10^4 [s⁻¹]
-2.00	0.0778	0.26	16.03	0.034	118.61	0.580	0.0015
-1.80	0.0612	0.51	14.01	0.031	96.03	0.677	0.0033
-1.50	0.0408	1.10	11.43	0.026	67.65	0.778	0.0085
-1.40	0.0351	1.37	10.64	0.024	59.48	0.795	0.0109
-1.20	0.0252	2.02	9.22	0.020	44.52	0.802	0.0162
-1.00	0.0172	2.76	8.05	0.017	32.54	0.748	0.0206
-0.80	0.0108	3.53	7.02	0.014	22.75	0.642	0.0227
-0.50	0.0042	4.57	5.82	0.009	12.12	0.389	0.0177
-0.40	0.0026	4.85	5.52	0.007	9.63	0.286	0.0138
-0.30	0.0015	5.07	5.25	0.005	7.63	0.184	0.0093
-0.25	0.0010	5.17	5.17	0.004	6.87	0.134	0.0070
-0.20	0.0006	5.24	5.06	0.003	6.18	0.092	0.0048
-0.15	0.0004	5.30	4.98	0.003	5.66	0.054	0.0028
-0.10	0.0002	5.34	4.90	0.002	5.22	0.025	0.0013
0	0.0000	5.38	4.79	0.000	4.79	0.000	0.0000
0.10	0.0002	5.35	4.71	0.002	4.86	0.026	0.0014
0.15	0.0004	5.31	4.70	0.003	5.11	0.058	0.0031
0.20	0.0006	5.25	4.70	0.003	5.44	0.098	0.0052
0.25	0.0009	5.18	4.76	0.004	5.97	0.148	0.0077
0.30	0.0014	5.09	4.76	0.005	6.59	0.201	0.0103
0.40	0.0025	4.87	4.78	0.007	8.22	0.319	0.0155
0.50	0.0043	4.61	4.91	0.009	10.37	0.436	0.0200
0.80	0.0105	3.58	5.52	0.014	20.22	0.724	0.0258
1.00	0.0167	2.81	6.18	0.017	29.70	0.841	0.0236
1.20	0.0245	2.08	7.02	0.020	41.67	0.896	0.0186
1.40	0.0340	1.43	8.05	0.024	56.28	0.893	0.0127
1.50	0.0395	1.15	8.63	0.026	64.59	0.876	0.0100
1.80	0.0592	0.54	10.67	0.031	94.11	0.754	0.0040
2.00	0.0753	0.29	12.23	0.034	117.74	0.638	0.0018

Fractional rate constant calculated for **diCl** within ω_1 vibration: $\qquad k^{\omega_1}_{3CT \to 1CT} \qquad = \qquad$ **0.3012**

Figure S22. Computational parameters for the prediction of $k^{\omega_1}_{3CT \to 1CT}$ in **diCl**.

Table S17. Computational parameters for the prediction of $k^{\omega_1}_{3CT \to 1CT}$ in **diBr**.

A_j	$\Delta E_{\omega_1}[A_j]$	$p_{\omega_1}[A_j]$	$\Delta E_{3CT-1CT}[A_j]$	$V_{3CT \to 1CT}[A_j]$	$\lambda_{3CT \to 1CT}[A_j]$	$k_{\omega_1}[A_j]$	$k_{\omega_1}[A_j] \cdot p_{\omega_1}[A_j]$
	[eV]	[%]	[meV]	[cm^{-1}]	[meV]	10^4 [s^{-1}]	10^4 [s^{-1}]
-2.00	0.0842	0.21	12.54	0.028	91.31	0.628	0.0013
-1.80	0.0659	0.43	11.16	0.025	73.74	0.691	0.0030
-1.50	0.0435	1.02	9.33	0.021	51.98	0.732	0.0075
-1.40	0.0373	1.30	8.79	0.020	45.84	0.728	0.0095
-1.20	0.0265	1.97	7.81	0.017	35.07	0.692	0.0137
-1.00	0.0178	2.77	6.97	0.014	26.19	0.616	0.0171
-0.80	0.0110	3.61	6.23	0.011	17.88	0.523	0.0189
-0.50	0.0040	4.75	5.41	0.007	10.17	0.295	0.0140
-0.40	0.0024	5.04	5.17	0.006	8.31	0.213	0.0107
-0.30	0.0013	5.28	5.01	0.004	6.88	0.133	0.0070
-0.25	0.0008	5.37	4.90	0.004	6.25	0.098	0.0052
-0.20	0.0005	5.44	4.84	0.003	5.76	0.065	0.0036
-0.15	0.0002	5.49	4.79	0.002	5.37	0.038	0.0021
-0.10	0.0001	5.53	4.73	0.001	5.04	0.018	0.0010
0	0.0000	5.54	4.63	0.000	4.63	0.000	0.0000
0.10	0.0002	5.49	4.53	0.001	4.61	0.018	0.0010
0.15	0.0005	5.41	4.53	0.002	4.70	0.041	0.0022
0.20	0.0010	5.33	4.54	0.003	4.93	0.072	0.0038
0.25	0.0015	5.23	4.55	0.004	5.24	0.108	0.0057
0.30	0.0020	5.12	4.57	0.004	5.62	0.151	0.0077
0.40	0.0034	4.85	4.65	0.006	6.66	0.245	0.0119
0.50	0.0052	4.52	5.03	0.007	8.11	0.342	0.0155
0.80	0.0129	3.35	5.44	0.011	14.72	0.611	0.0205
1.00	0.0201	2.53	5.99	0.014	21.20	0.744	0.0188
1.20	0.0291	1.78	6.33	0.017	29.49	0.830	0.0148
1.40	0.0401	1.16	6.67	0.020	39.74	0.870	0.0101
1.50	0.0464	0.91	7.05	0.021	45.65	0.874	0.0079
1.80	0.0689	0.38	8.44	0.025	67.93	0.808	0.0031
2.00	0.0871	0.19	9.47	0.028	85.18	0.738	0.0014

Fractional rate constant calculated for **diBr** within ω_1 vibration: $\quad k^{\omega_1}_{3CT \to 1CT} \quad = \quad$ **0.2381**

Figure S23. Computational parameters for the prediction of $k^{\omega_1}_{3CT \to 1CT}$ in **diBr**.

**Table S18**. Computed fractional rate constant within vibrational model via direct ^{3}CT-^{1}CT transition.

|	Fractional constant rates			Contribution of each mode to total $k_{3CT \to 1CT}$		
	$k_{3CT \to 1CT}^{\omega_i}$ [10^4 s^{-1}][a]			$\mu_{3CT \to 1CT}^{\omega_i}$ [%][b]		
i	**H**	**diCl**	**diBr**	**H**	**diCl**	**diBr**
1	0.4923	0.3012	0.2381	87.3	57.7	21.6
2	0.0004	0.0042	0.0105	0.1	0.8	1.0
3	0.0032	0.0771	0.0038	0.6	14.7	0.3
4	0.0104	0.0259	0.2078	1.8	4.9	18.8
5	0.0004	0.0507	0.0528	0.1	9.7	4.8
6	0.0007	0.0041	0.0287	0.1	0.8	2.6
7	0.0025	0.0058	0.0216	0.4	1.1	2.0
8	0.0542	0.0535	0.5403	9.6	10.2	49.0
$k_{3CT \to 1CT}$ [10^4 s^{-1}][c]	**0.5641**	**0.5236**	**1.1036**			

[a] – calculated using equation (S34);
[b] – calculated using equation (S42);
[c] – calculated using equation (S33).
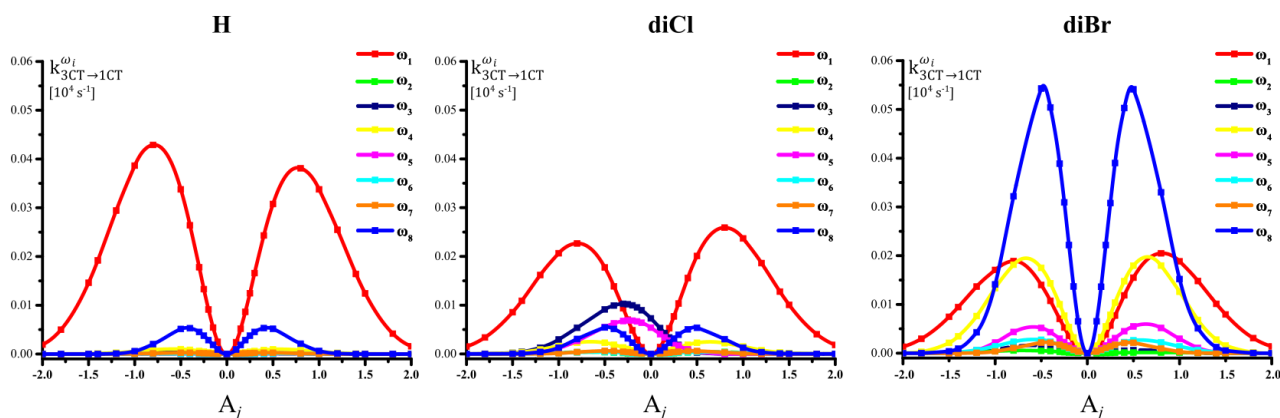
Figure S24. Computed fractional rates $k_{3CT \to 1CT}^{\omega_i}$ for various vibrational modes.
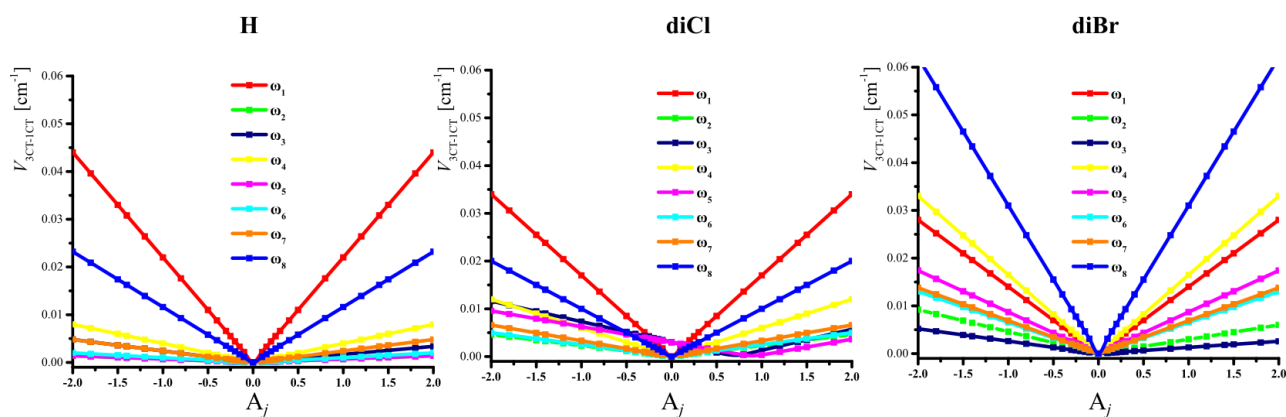
Figure S25 Computed SOC dependences on amplitudes A_j of various vibrational modes.

Section S8: The assumptions towards rotational-vibronic model of direct ^{3}CT-^{1}CT transition

Analysis of the results obtained by rotational and vibronic models can lead to the following conclusions. The rotational model describes SOC enhancement of the ^{3}CT-^{1}CT transition thanks to the specific molecular rotations – deviations of the θ dihedral angle. Such a model thus reflects the structural diversity of emitter in macroscopic condenced medium and takes into account only most important conformations – θ-rotamers. The rotational model seems to be optimal solution for the description of photophysics of light-atom emitters with orthogonal structure.

The presented vibronic model describes further SOC enhancement of the ^{3}CT-^{1}CT transition in selected emitter molecule (θ-rotamer) thanks to the low-energy molecular vibrations. Analysis of the effect of relatively low-amplitude atomic movements on the electronic structure provides fine prediction of SOC, energy gaps and finally spin-flip rate constants.

Obviously, complete TADF model should combine such rotational and vibronic models. For all θ-rotamers existing at room temperature, the effect of molecular vibrations on the electronic structure should be analyzed quantitatively. This task is, however, extremely time-consuming and computationally expensive.

To approximate such a rotational-vibronic model, we assumed that vibrational SOC enhancement in the 90°-rotamer is similar to that in other θ-rotamers. To estimate the value of such enhancement, relative contribution of transition via the ω_1 rotational channel versus all vibrational channels was used: $\mu_{3CT \to 1CT}^{\omega_1} = \frac{k_{3CT \to 1CT}^{\omega_1}}{\sum_{i=1}^{n} k_{3CT \to 1CT}^{\omega_i}}$, calculated for the 90°-rotamers of **H**, **diCl**, and **diBr** (**Table S18**). The statistical sum of $k_{3CT \to 1CT}$ obtained from rotational model (**Tables S15-S17**) was divided by the $\mu_{3CT \to 1CT}^{\omega_1}$ giving rotational-vibronic values of $k_{3CT \to 1CT}$ presented in **Table S19**. Such values showed the best correlation with the experimental rISC rate constants confirming the correctness of the above mentioned assumptions.

Table S19. Summary of developed theoretical models and comparasion with experimental results.

|	Experimental[a] k_{rISC} $[10^4 \text{ s}^{-1}]$		Theoretical models $\text{k}_{3CT \to 1CT}$ $[10^4 \text{ s}^{-1}]$		
	ZNX	PMMA	"Rotational"[b]	"Vibrational"[c]	"Rotational-vibronic"
H	1.03	2.92	2.81	0.56	3.22
diCl	0.87	1.85	1.75	0.52	3.07
diBr	1.74	8.23	1.09	1.10	5.05

[a] - experimental determination of rate constant described in **Section S3: Determination of photophysical parameters**;

[b] - prediction of rate constant within "rotational" model described in **Section S6: Computational details for prediction rISC** rate constant **within rotational model via direct ^{3}CT-^{1}CT transition**;

[c] - prediction of rate constant within "vibrational" model described in **Section S7: Computational details for the prediction of rISC** rate constant **within rotational model via direct ^{3}CT-^{1}CT transition**.

Section S9: Molecular electronic orbitals

Molecular orbitals involved in the formation of key excited electronic states are presented below.
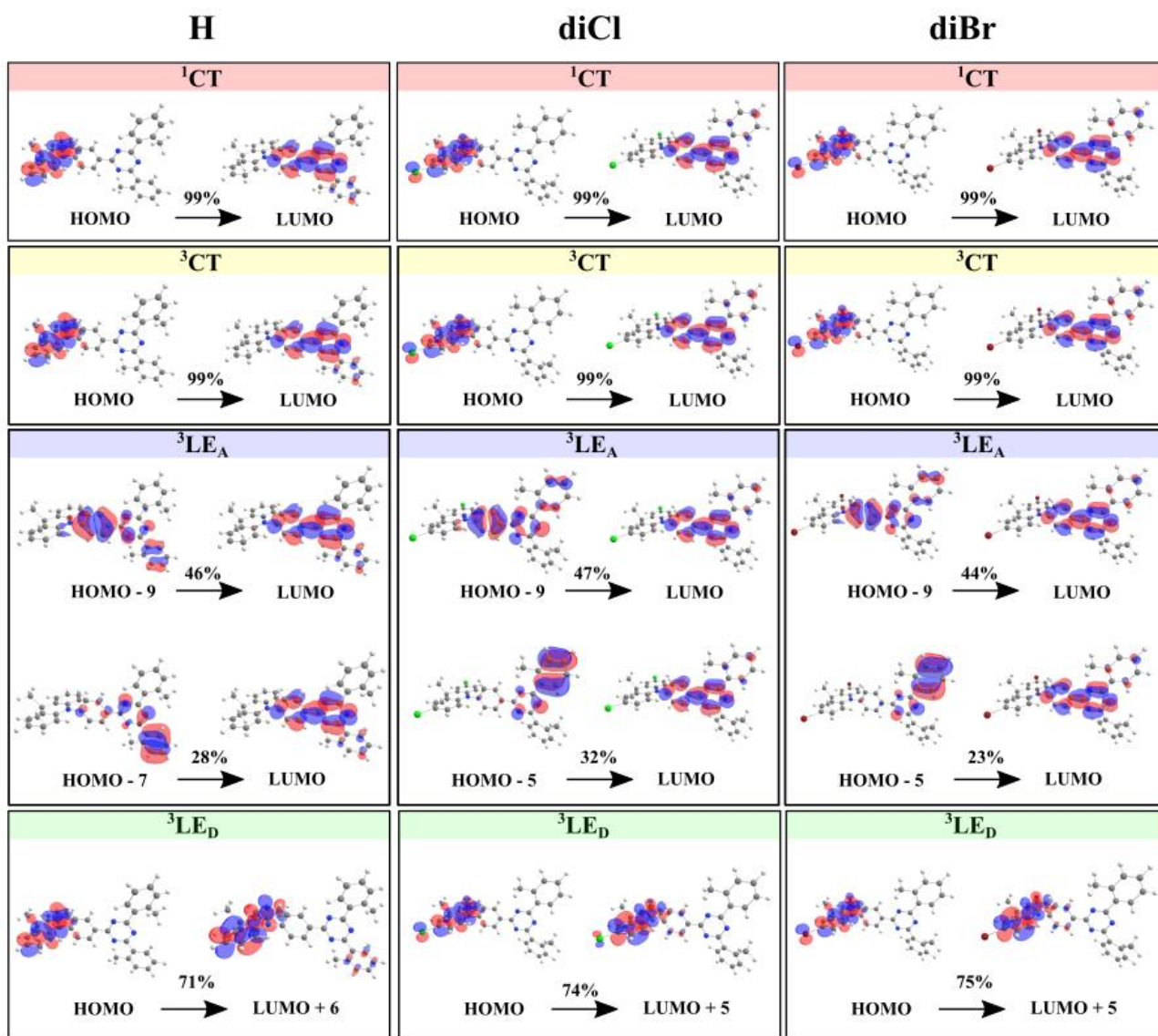
Figure S26. Computed MOs

As can be seen from the respective MO, the 1CT and 3CT states are formed via electron density transfer from DMAC donor to aryl-s-triazine acceptor. The ^3LE_A state is formed due to redistribution of electronic density within the acceptor fragment. The ^3LED state is formed due to redistribution of electronic density within the donor fragment. These data support the conclusions made on the basis of spectral analysis in main text and page S4-S5.

REFERENCES

[S1] Dias, F. B.; Penfold, T. J.; Monkman, A. P. Photophysics of thermally activated delayed fluorescence molecules. *Methods Appl. Fluoresc*. **2017**, *5*, 012001.

[S2] Stavrou, K.; Franca L. G.; Monkman, A. P. Photophysics of TADF Guest-Host Systems: Introducing the Idea of Hosting Potential. *ASC Appl. Electron. Mater.* **2020**, *2*, 2868 – 2881.

[S3] Serdiuk, I. E.; Mońka, M.; Kozakiewicz, K.; Liberek, B.; Bojarski, P.; Park, S. Y. Vibrationally Assisted Direct Intersystem Crossing between the Same Charge-Transfer States for Thermally Activated Delayed Fluorescence: Analysis by Marcus-Hush Theory Including Reorganization Energy. *J. Phys Chem. B* **2021**, *125*, 2696 – 2706.

[S4] Tao, Y.; Yuan, K.; Chen, T.; Xu, P.; Li, H.; Chen, R.; Zheng, C.; Zhang, L.; Huang, W. Thermally Activated Delayed Fluorescence Materials Towards the Breakthrough of Organoelectronics. *Adv. Mater.* **2015**, *26*, 7931 – 7958.

[S5] IUPAC. Compendium of Chemical Terminology, 2nd ed. (the "Gold Book"). Compiled by A. D. McNaught and A. Wilkinson. Blackwell Scientific Publications, Oxford (1997). Online version (2019-) created by S. J. Chalk. ISBN 0-9678550-9-8. https://doi.org/10.1351/goldbook.